

Directional Josephson traveling-wave parametric amplifier via non-Hermitian topology

Tomás Ramos,^{1,*} Álvaro Gómez-León,¹ Juan José García-Ripoll,¹ Alejandro González-Tudela,¹ and Diego Porras^{1,†}

¹*Institute of Fundamental Physics IFF-CSIC, Calle Serrano 113b, 28006 Madrid, Spain.*

Low-noise microwave amplification is crucial for detecting weak signals in quantum technologies and radio astronomy. An ideal device must amplify a broad range of frequencies while adding minimal noise, and be directional, so that it favors the observer's direction while protecting the source from its environment. Current amplifiers do not satisfy all these requirements, severely limiting the scalability of superconducting quantum devices. Here, we demonstrate the feasibility of building a near-ideal quantum amplifier using a homogeneous Josephson junction array and the non-trivial topology of its dynamics. Our design relies on breaking time-reversal symmetry via a non-local parametric drive, which induces directional amplification in a way similar to edge states in topological insulators. The system then acquires unprecedented amplifying properties, such as a gain growing exponentially with system size, exponential suppression of back-wards noise, and topological protection against disorder. We show that these features allow a state-of-the-art superconducting device to manifest near-quantum-limited directional amplification with a gain largely surpassing 20 dB and -30 dB of reverse attenuation over a large bandwidth of GHz. This opens the door for integrating near-ideal and compact pre-amplifiers on the same chip as quantum processors.

Low-noise amplification enables high-sensitivity applications ranging from astronomic instrumentation [1] to nano-mechanical sensing [2]. In superconducting quantum technology [3, 4], in particular, microwave signals carrying quantum information are so weak that near quantum-limited amplification is indispensable to detect them in a single-shot measurement [5–7]. In this respect, the most advanced amplifiers currently available are Josephson traveling-wave parametric amplifiers (JTWPAs) which are built of a carefully engineered array of Josephson junctions (JJs) [8–11]. Activating the Kerr non-linearities via four-wave-mixing [12, 13], these devices have demonstrated a great amplification performance with gains above 20 dB, near quantum-limited noise, and a large bandwidth in the GHz range [14]. An important drawback is that JTWPAs are not truly directional, meaning that parasitic signals and vacuum fluctuations can be back-amplified and contaminate the quantum source. In practice, this is avoided by equipping the JTWPAs with isolators, but these are bulky and lossy external elements that limit the efficiency and scalability of superconducting quantum devices.

Directional amplification has only been realized on few-mode non-reciprocal devices [15–20], which are fundamentally narrowband. Broadband amplification is crucial towards implementing large-scale quantum information processors, where multiple signals need to be multiplexed and simultaneously detected [21]. Therefore, unifying the broadband properties of JTWPAs with the compactness of a directional amplifier with built-in backwards isolation is one of the holy grails in the field [14].

In this work, we extend concepts of topological photonics [22, 23] and topological amplification [24–27] to render a JTWPA directional and non-reciprocal, while retaining all its excellent amplifying properties of gain, noise, and bandwidth. The key to build a topological JTWPA is to perform the four-wave-mixing process indirectly via an auxiliary resonator array [see Fig. 1(a,b)]. With an adequate choice of parameters, this auxiliary array supports a classical running wave which distributes an homogeneous coherent drive

along the JJ array. The phase ϕ of this wave provides perfect phase matching without dispersion engineering and, most remarkably, it induces a synthetic gauge field that breaks time-reversal symmetry (TRS) without requiring Floquet engineering [28] nor external magnetic fields. The combination of this gauge field, non-local parametric pump induced by Kerr nonlinearities, and homogeneous local dissipation, allows us to stabilize a steady-state with topological amplifying properties. In this driven-dissipative phase, the topological JTWPA exhibits directional and near-quantum-limited amplification of microwave signals with a gain that grows exponentially with the array size while keeping a large bandwidth on the order of the array hopping. The directionality is manifested by an exponential suppression of all backwards added noise and signals propagating towards the source. Moreover, the device has topological protection against disorder in all system parameters and, in particular, to imperfections inherent in the fabrication of JJs [29].

Beyond proposing the design of this novel topological JTWPA, we also characterize its performance at various operation points, and demonstrate the feasibility to implement it with current superconducting circuit technology [30–32]. We predict that a device with $N \lesssim 30$ sites can provide near quantum-limited amplification over a bandwidth of GHz with more than 20 dB of gain and -30 dB of backwards attenuation. This is two orders of magnitude larger in bandwidth and directionality than previous non-reciprocal amplifiers [15–20]. Our work thus provides a promising route towards the scalable integration of near-ideal pre-amplifiers and quantum processors on the same on-chip, avoiding the use of external isolators.

TOPOLOGICAL JOSEPHSON TRAVELING WAVE PARAMETRIC AMPLIFIER

Fig. 1(a,b) displays the superconducting circuit scheme and the associated quantum optics model to realize a topological JTWPA. It consists of a homogeneous JJ array of N sites

(blue) that is coupled to local input/output ports on each site (grey), as well as to an auxiliary array of linear resonators (red). The backbone of the setup is the JJ array, where an arrangement of capacitors and JJs induce localized microwave modes a_j that are coupled via linear and non-linear terms [cf. Fig. 1(a)-(b), blue]. The dynamics of these anharmonic modes is described by the real-space Hamiltonian

$$H_{\text{JJA}} = \omega_a \sum_j a_j^\dagger a_j + J_a \sum_j (a_{j+1}^\dagger a_j + \text{h.c.}) - \frac{K_s}{2} \sum_j a_j^\dagger a_j^\dagger a_j a_j - K_c \sum_j a_{j+1}^\dagger a_{j+1} a_j^\dagger a_j, \quad (1)$$

with ω_a the on-site frequencies, J_a the nearest neighbour hopping between sites, and K_s , K_c the self- and cross-Kerr nonlinear couplings. These JJ arrays have been extensively studied for implementing JTWPAs, but they are typically built with inhomogeneous parameters in order to achieve phase matching of waves via dispersion engineering [8–11, 33]. This is not necessary in our homogeneous implementation as we show below. Another non-standard consideration of our design is that we consider both inter- and intra-site JJs [cf. Fig. 1(a), blue], which allows us to control the ratio K_s/K_c . Further details on our specific JJ array, including a relation between the effective model (1) and the microscopic circuit quantities is given in Methods.

The second important ingredient are input/output ports to insert and retrieve microwave signals on the JJ array, which we realize by capacitively coupling 50Ω transmission lines on each site j [cf. Fig. 1(a), grey]. Although we will typically send the quantum signal on the first site $j = 1$ and retrieve the amplified field on the last site $j = N$ [cf. Fig. 1(a,b)], our setup requires an homogeneous arrangement of output ports in order to induce the same local decay κ on all modes a_j . This is non-standard in JJ arrays, and it will allow us to stabilize the topological amplifier steady-state phase.

The final and key ingredient to realize a topological JTWPA is to perform four-wave-mixing indirectly by sending a strong pump Ω_b through a waveguide and use its propagation phase ϕ to break TRS. We implement this in our setup by capacitively coupling the JJ array to an auxiliary chain of linear superconducting resonators b_j , on which we add input/output ports at both boundaries b_1 and b_N [cf. Fig. 1(a,b), red]. The mechanism for breaking TRS works as follows. First, the dynamics of the auxiliary array is given by a tight-binding Hamiltonian,

$$H_{\text{aux}} = \omega_b \sum_j b_j^\dagger b_j + J_b \sum_j (b_{j+1}^\dagger b_j + \text{h.c.}) + J_{ab} \sum_j (a_j^\dagger b_j + \text{h.c.}), \quad (2)$$

with ω_b the on-site frequencies, J_b the intra-array hopping, and J_{ab} the local couplings to the JJ array. Second, we use the input port on site b_1 to apply a strong and resonant pump, $H_{\text{aux}}^{(p)} = 2i\Omega_b(b_1 + b_1^\dagger)\cos(\omega_b t)$, which inputs a large stream of photons on the first site. Third, we force these photons

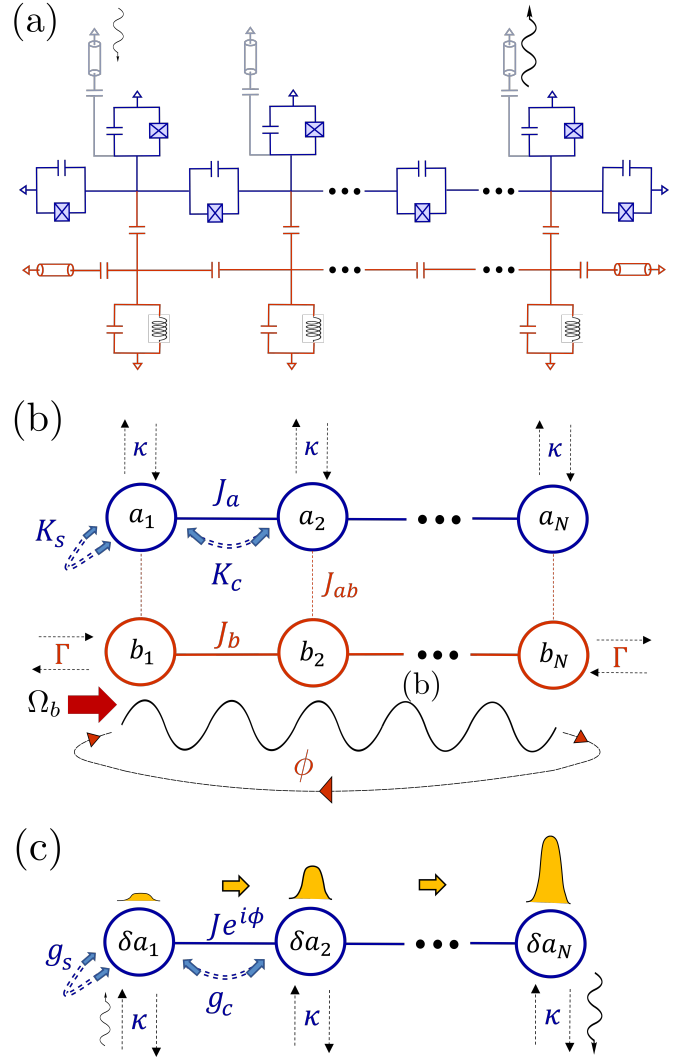


FIG. 1. Realization of a topological Josephson traveling-wave parametric amplifier (JTWPA). (a) Superconducting circuit scheme composed of a JJ array (blue), where each site $j = 1, \dots, N$ is coupled to a 50Ω input/output line (grey), and to an auxiliary array of linear superconducting resonators (red). All couplings are capacitive and linear except for the JJ array, where Josephson junctions mediate nonlinear Kerr interactions. (b) Quantum optics model implemented by the superconducting circuit in (a). The JJ array describes a nonlinear array of modes a_j with self- and cross-Kerr couplings K_s and K_c , as well as linear hopping J_a . In contrast, the local modes of the auxiliary array b_j are only linearly coupled via intra- and inter-array couplings J_b and J_{ab} , respectively. Transmission lines provide a local decay κ to each a_j mode, and a $\Gamma = 2J_b$ decay to auxiliary modes at the boundaries, b_1 and b_N . The mode b_1 is coherently driven with strength Ω_b to generate a classical right-moving running-wave of phase $\phi = \pi/2$, which is used to perform indirect four-wave-mixing on the JJ array and break time-reversal symmetry (see text). (c) Effective linear model describing topological parametric amplification. The combination of complex hopping $J e^{i\phi}$, local decay κ , and parametric pumping terms g_s and g_c , leads the system to a topological steady-state phase, where external signals entering at site $j = 1$ are directionally amplified and accumulate at the right boundary $j = N$.

to propagate to the right along the auxiliary array by making the inter-array coupling highly off-resonant $J_{ab} \ll |\omega_a - \omega_b|$. Fourth, we set a local decay of $\Gamma = 2J_b$ at both output ports of the auxiliary array, which provides perfect impedance matching for the photons to leak out without reflections at the boundaries. Under the above conditions, the auxiliary array behaves as a nearly classical waveguide, and its steady-state supports a right-moving running-wave with well-defined phase $\phi = \pi/2$ (see Methods):

$$\langle b_j \rangle \approx \frac{i\Omega_b}{2J_b} e^{-i(\phi j + \omega_b t)}. \quad (3)$$

Remarkably, this running-wave distributes an effective coherent pump on all sites of the JJ array, $H_{JJ}^{(p)} \approx i\Omega_a \sum_j a_j^\dagger e^{-i(\phi j + \omega_b t)} + \text{h.c.}$, whose amplitude $\Omega_a = (J_{ab}/2J_b)\Omega_b$ is homogeneous and whose phase ϕ breaks TRS. For a sufficiently strong pump, this allows us to perform four-wave-mixing on the JJ array, and displace all local modes as $a_j = (\alpha + \delta a_j) e^{-i(\phi j + \omega_b t)}$, where $\delta a_j(t)$ describe quantum fluctuations around a large mean field displacement $|\alpha|^2 \gg \langle \delta a_j^\dagger \delta a_j \rangle$. Notice that the spatially varying phase imprinted by the pump provides perfect phase matching on the JJ array, so that α is the same on all sites and satisfies an homogeneous non-linear steady-state equation, $(\kappa/2 - i[\omega_b - \omega_a + (K_c + K_s)|\alpha|^2])\alpha = \Omega_a$ (see Methods). Furthermore, the dynamics of the quantum fluctuations δa_j becomes approximately linear and implements a topological JTWP with effective Hamiltonian [cf. Fig. 1(c)],

$$H_{\text{pa}} = \sum_{j,l} \mathcal{M}_{jl} \delta a_j^\dagger \delta a_l - \sum_{j,l} \frac{\mathcal{K}_{jl}}{2} (\delta a_j^\dagger \delta a_l^\dagger + \text{h.c.}). \quad (4)$$

Here, photon-conserving interactions, $\mathcal{M}_{jl} = -\Delta \delta_{jl} + J(e^{-i\phi} \delta_{j+1,l} + e^{i\phi} \delta_{j-1,l})$, contain complex hopping terms with the phase ϕ playing the role of an artificial gauge field [28]. The strong external pump also induces a shift on the effective hopping strength $J = J_a + 2K_c|\alpha|^2$ and on-site detuning $\Delta = \omega_b - \omega_a + 2(K_s + K_c)|\alpha|^2$, which is proportional to the mean photon number $|\alpha|^2$. The second term in Eq. (4) describes local and non-local two-photon parametric pumping processes, $\mathcal{K}_{jl} = g_s \delta_{jl} + g_c(\delta_{j+1,l} + \delta_{j-1,l})$, which are induced by the self- and cross-Kerr nonlinearities as $g_s = (K_s - K_c)|\alpha|^2$ and $g_c = K_c|\alpha|^2$. These terms are responsible for generating amplification of microwave signals, which in combination with the complex hopping $J e^{i\phi}$ and the homogeneous dissipation κ leads to directional amplification when the right parameter regime is met.

DIRECTIONAL AMPLIFICATION VIA TOPOLOGY

To identify the conditions under which the steady state of the system stabilizes a topological amplifying phase, we need to consider the complete driven-dissipative dynamics of the quantum fluctuations $\delta a_j(t)$. In the Heisenberg picture, this

can be conveniently written in linear matrix form as,

$$\delta \dot{\vec{a}}(t) = -i H_{\text{nh}} \delta \vec{a}(t) - \sqrt{\kappa} \vec{a}_{\text{in}}(t), \quad (5)$$

where $\delta \vec{a}(t) = [\delta a_j(t), \delta a_j^\dagger(t)]^T$ is the vector of quantum fluctuations, and $\vec{a}_{\text{in}}(t) = [a_j^{\text{in}}(t), a_j^{\text{in}\dagger}(t)]^T$ the vector of input operators describing the signal and/or noise fields entering the amplifier at any of its sites j [cf. Fig. 1(c)]. Importantly, the $2N \times 2N$ non-Hermitian matrix H_{nh} describes interactions, pumping, and dissipative processes in an unified way,

$$H_{\text{nh}} = \begin{pmatrix} \mathcal{M}_{jl} - i\frac{\kappa}{2}\delta_{jl} & -\mathcal{K}_{jl} \\ \mathcal{K}_{jl} & -\mathcal{M}_{jl}^* - i\frac{\kappa}{2}\delta_{jl} \end{pmatrix}, \quad (6)$$

and it contains all information about the dynamical and spectral properties of the amplifier, as well as the stability and topology of the steady-state [see supplementary material (SM)]. For instance, in terms of the Green's function matrix $G(\omega) = (\omega - H_{\text{nh}})^{-1}$, we can determine the amplifier's gain $\mathcal{G}_j = \kappa^2 |G_{j1}(\omega_s)|^2$ for a signal of frequency ω_s entering at site 1 and leaving at any site $j > 1$. Similarly, the reverse gain from site $j > 1$ to 1 is given by $\mathcal{G}_j^{(R)} = \kappa^2 |G_{1j}(\omega_s)|^2$. Note that we are operating the device as a phase-preserving amplifier and that all frequencies ω and ω_s are taken with respect to the pump ω_b .

In a topologically non-trivial steady-state phase, the Green's function components become asymmetric, $G_{jl} \neq G_{lj}$, and therefore the amplification is non-reciprocal. To see for which parameters this indeed occurs, we rely on a connection between open quantum systems and topological band theory that we developed in Refs. [25, 27, 34]. This consists in constructing an artificial hermitian Hamiltonian $\mathcal{H}(\omega)$ from the non-hermitian H_{nh} matrix as,

$$\mathcal{H}(\omega) = \begin{pmatrix} 0 & \omega - H_{\text{nh}} \\ \omega - H_{\text{nh}}^\dagger & 0 \end{pmatrix}, \quad (7)$$

and relating the eigenvalue problem of $\mathcal{H}(\omega)$ to the true steady-state properties and Green's functions of the amplifier array. In particular, if the system parameters are such that $\mathcal{H}(\omega)$ is in a topologically non-trivial phase (according to the ten-fold way [35, 36]), its eigen-spectrum $E_n(\omega)$ manifests pairs of zero-energy modes whose energy is exponentially suppressed, $E_0(\omega) \sim \pm e^{-N\zeta(\omega)}$, with ζ the inverse localization length. As shown in Fig. 2(a), these zero-energy modes appear within a topological band-gap Δ_{top} and also within a topological bandwidth w_{top} , since the topological region is frequency dependent. Inside this region, defined as $E_0(\omega) \leq 1/N$ for a finite system, the associated zero-energy eigenstates of $\mathcal{H}(\omega)$ are exponentially localized edge states, which induce an exponential spatial dependence on the physical Green's functions $G_{jl}(\omega)$ of the system as (see SM),

$$G_{jl}(\omega) \approx e^{(j-l)\zeta(\omega)} G_{11}(\omega), \quad j > l. \quad (8)$$

Directional amplification follows directly from this fact since the gain of the topological amplifier grows exponentially from

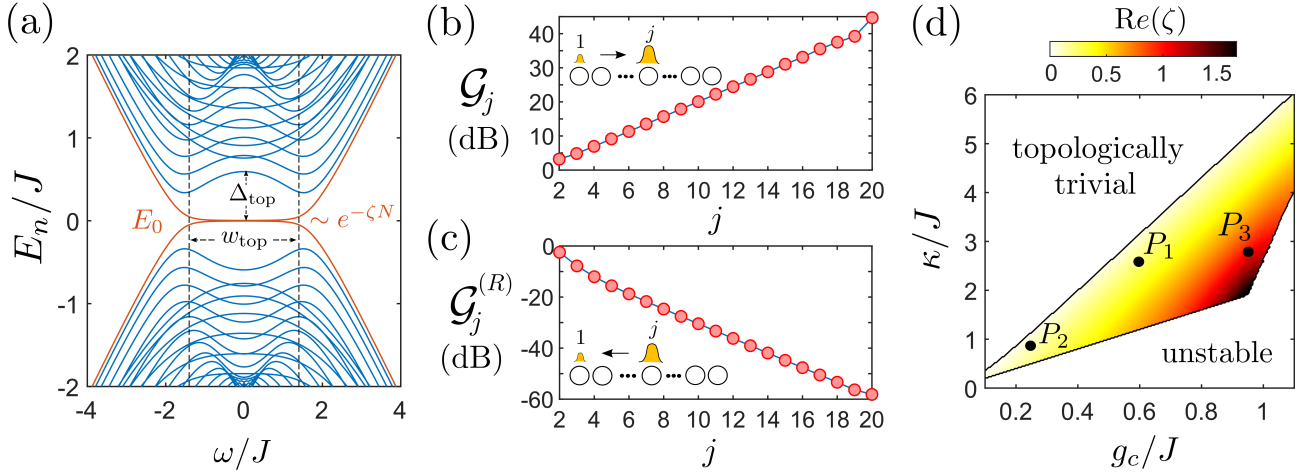


FIG. 2. **Directional amplification in a topological JTWP.** (a) Eigen-spectrum E_n of the extended Hamiltonian $\mathcal{H}(\omega)$ in Eq. (7) as function of frequency ω . In a topologically non-trivial steady state, $E_n(\omega)$ manifests pairs of zero-energy modes $E_0(\omega) \sim \pm e^{-N\zeta(\omega)}$ (in red) within a topological band-gap of size Δ_{top} and a topological bandwidth w_{top} . (b) Exponential growth of the gain \mathcal{G}_j (in dB) for a signal of frequency $\omega_s = -0.5J$ entering at site 1 and leaving at site j . (c) Exponential suppression of the reverse gain $\mathcal{G}_j^{(R)}$ (in dB) for the same signal propagating backwards from site j to the first site 1. (d) Phase diagram as function of κ/J and g_c/J indicating the region for stable topological steady-state phases. The color bar shows the inverse localization length $\text{Re}[\zeta] > 0$, which determines the strength of the topological amplification (see text). The black dots indicate the three operation points we consider in this work. P_1 corresponds to $g_c/J = 0.6$ and $\kappa/J = 2.6$, P_2 to $g_c/J = 0.25$ and $\kappa/J = 0.9$, and P_3 to $g_c/J = 0.95$ and $\kappa/J = 2.8$. Other parameters are $g_s/g_c = 1$, $\Delta = 0$, $\phi = \pi/2$, $\omega = -0.5J$, and $N = 20$. Parameters P_1 are used in panels (a)-(c).

left to right $\mathcal{G}_j \approx e^{2(j-2)\text{Re}(\zeta)}\mathcal{G}_2$, while back-wards propagating signals are exponentially suppressed with distance. Figs. 2(b)-(c) demonstrate numerically this behaviour for a signal of frequency $\omega_s = -0.5J$ and the same parameters as in Fig. 2(a). Due to the exponential scaling of the gain, a topological JTWP of just $N = 20$ sites reaches more than 40 dB of amplification and -60 dB of reverse attenuation. Note that small deviations from the exponential dependence near the boundaries are due to finite size effects.

Looking for edge states in $\mathcal{H}(\omega)$ allows for a systematic study of the steady-state phases supporting directional amplification. Fig. 2(d) displays a phase diagram of the system as a function of g_c/J and κ/J , for given parameters $g_s/g_c = 1$, $\omega/J = -0.5$, $\Delta = 0$, $\phi = \pi/2$, and $N = 20$. The colored region indicates the topological amplifying phase, which requires a balance between parametric drive g_c and decay κ : For too large decay, the system becomes topologically trivial and for too large drive it becomes unstable. Stability of the steady-state is an essential requisite for the experimental realization of the topological JTWP, which is guaranteed when all eigenvalues of H_{nh} have negative imaginary parts [25, 27]. In addition, the color bar in Fig. 2(d) displays the inverse localization length $\text{Re}[\zeta]$ which determines the exponent of the gain in the topological phase. Note that larger $\text{Re}[\zeta]$ is not always better as this depends on the application of the amplifier. In this work, we consider three working points as indicated in Fig. 2(d). Parameters P_1 are used in panels (a)-(c) of Figs. 2, whereas P_2 and P_3 are used below when discussing the performance of the amplifier. Notice that we always consider $g_s/g_c = 1$, which is realized by setting $K_s = 2K_c$.

PERFORMANCE OF THE DIRECTIONAL AMPLIFIER

Similarly to Josephson parametric amplifiers (JPA) [12, 37], the gain of the topological JTWP cannot grow indefinitely because quantum fluctuations become highly populated $\langle \delta a_j^\dagger(t) \delta a_j(t) \rangle \gtrsim |\alpha|^2$, and saturate the linear response of the system. Indeed, when amplifying a coherent signal of frequency ω_s entering at site 1, the occupation at site $j > 1$ oscillates in time reaching a maximum (see SM):

$$\max \langle \delta a_j^\dagger \delta a_j \rangle = \kappa |\alpha_s|^2 (|G_{j1}(\omega_s)| + |G_{j,N+1}(-\omega_s)|)^2 + \frac{1}{2\pi\kappa} \int d\omega n_j(\omega). \quad (9)$$

The first term is proportional to the input flux $|\alpha_s|^2$ and originates from coherent photons in signal and idler fields. In contrast, the second term describes incoherent photons generated by the amplifier with a density $n_j(\omega) = \kappa^2 \sum_l |G_{j,N+l}(\omega)|^2$ per unit frequency. This noise is fundamentally bounded by $n_j^{\text{add}}(\omega) = n_j(\omega)/\mathcal{G}_j(\omega) \geq 1$, with $n_j^{\text{add}}(\omega)$ the added noise [38], and thus it is always present in a quantum amplifier. In the topological phase, the Green's function anomalous components $G_{j,N+l}$ behave exponentially as G_{jl} in Eq. (8) and, therefore, $\max \langle \delta a_j^\dagger \delta a_j \rangle$ also grows exponentially from left to right [cf. Fig. 3(a)]. On the one hand, this directional growth is a steady-state signature of topological amplification as it indicates the accumulation of photons at one boundary of the system [cf. Fig. 1(c)]. On the other hand, this fast growth also limits the size N in which the amplifier avoids saturation, $\langle \delta a_N^\dagger \delta a_N \rangle / |\alpha|^2 \ll 1$. Nevertheless, a compact topological

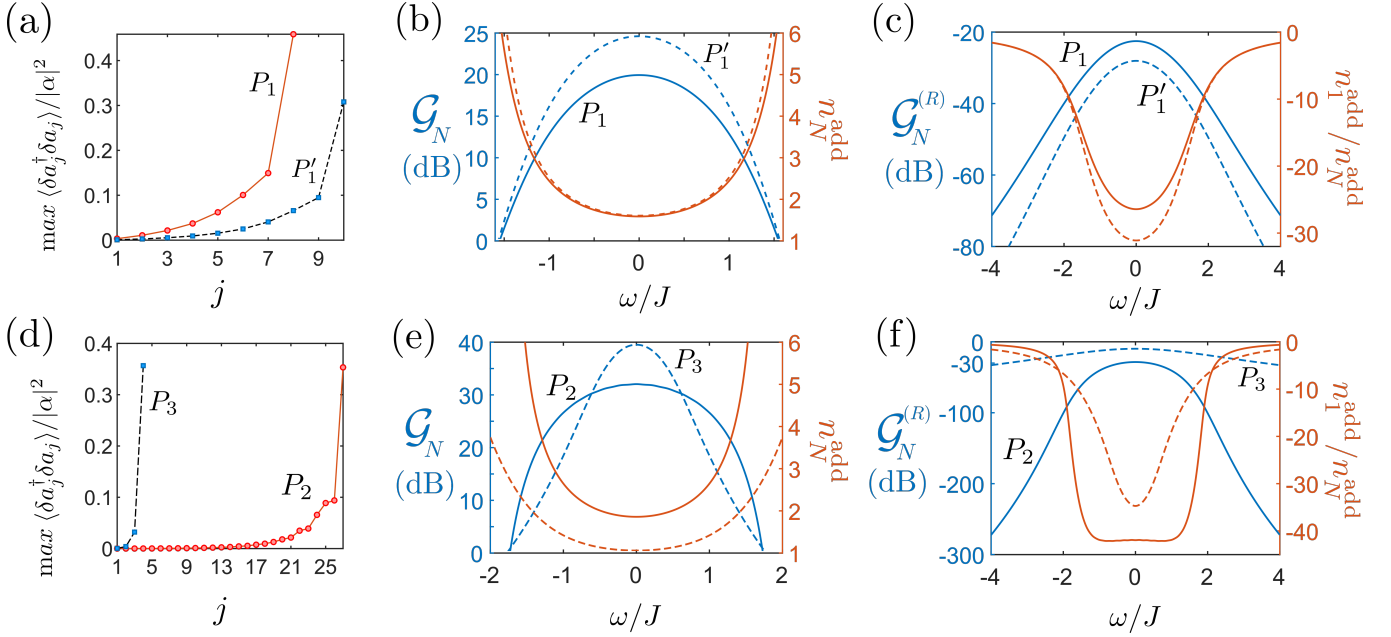


FIG. 3. **Broadband performance of the topological JTWP.** (a) Normalized maximum occupation $\langle \delta a_j^\dagger(t) \delta a_j(t) \rangle / |\alpha|^2$ as function of array site j when amplifying a signal of flux $|\alpha_s|^2 = 0.03J$ and frequency $\omega_s = -0.5J$. (b) Frequency dependence of gain \mathcal{G}_N (blue) and added noise n_N^{add} (red) at the last array site $j = N$, represented on the left and right vertical axes, respectively. (c) Frequency dependence of reverse gain $\mathcal{G}_N^{(R)}$ at last site (blue) and noise asymmetry $n_N^{\text{add}}/n_N^{\text{add}}$ (red), represented on the left and right vertical axes, respectively. In panels (a)-(c), solid lines correspond to parameters P_1 with $N = 8$ and dashed line to P'_1 with $N = 10$. (d)-(f) Same quantities as in (a)-(c) but for $|\alpha_s|^2 = 0.05J$, and parameters P_2 (solid) and P_3 (dashed).

JTWP can still show an outstanding performance in all figures of merit as shown below.

Let us first consider the working point P_1 used in Fig. 2, which can be realized with circuit parameters similar to the ones in Ref. [31] (see details in Table I of Methods). For this parameter set, the device can avoid saturation up to a size of $N = 8$ when amplifying a signal of $|\alpha_s|^2/2\pi \sim 5$ MHz [cf. solid line in Fig. 3(a)]. To characterize the broadband performance of the directional amplification, we display in Figs. 3(b)-(c) the frequency dependence of the gain \mathcal{G}_N and reverse gain $\mathcal{G}_N^{(R)}$ (left axes in blue), as well as the added noise n_N^{add} and noise asymmetry $n_N^{\text{add}}/n_N^{\text{add}}$ (right axes in red). For parameters P_1 (solid lines), we find that the gain \mathcal{G}_N can reach 20 dB at the center with just 0.6 added photons above the quantum limit. Within the topological bandwidth of $w_{\text{top}} \sim 2J = 2\pi \cdot 310$ MHz, the gain is above 13 dB, reverse gain below -23 dB, and noise asymmetry below -22 dB, providing a strong protection to the quantum source that generates the signal. For a directional amplifier, this bandwidth is already one order of magnitude larger than what has been achieved so far [15–20], but for practical application it is desirable to provide at least 20 dB of gain over a bandwidth of GHz [14]. We show below that this is possible for a topological JTWP provided one uses a technique already developed for JPAs.

Increasing the gain, bandwidth, and dynamic range boils down to increasing the maximum $|\alpha|^2$ that the system can

sustain, but this is fundamentally restricted in JJ arrays by the low flux condition $|\phi_j^a| \ll \Phi_0$, which implies $|\alpha|^2 \ll (\Phi_0/2\phi_{zpf})^2$ [12, 30], with Φ_0 the flux quantum and ϕ_{zpf} the zero point fluctuation (see Methods). Since $\phi_{zpf} = \sqrt{\hbar/(2\omega_a C_a^{\text{eq}})}$, the naive solution is to increase the capacitance C_a^{eq} further, but in practice this is problematic as it generates parasitic geometrical inductances larger than the Josephson inductances themselves. Nevertheless, as proposed and experimentally demonstrated in Refs. [12, 30, 37], we can replace each JJ in the setup [cf. Fig. 1(a)] by a sub-array of M JJs in series (with a Josephson energy M times larger), and thereby reduce the flux drop across each JJ as $\phi_j^a \rightarrow \phi_j^a/M$ (see Fig. 5(b) of Methods). Remarkably, this allows the topological JTWP to sustain a mean displacement M^2 times larger, $|\alpha|^2 \ll M^2(\Phi_0/2\phi_{zpf})^2$, while keeping the same effective quantities in Eq. (4).

Implementing these sub-arrays of JJs has a dramatic improvement in the performance of the topological JTWP. To show this, we consider circuit parameters similar to the ones reported in Ref. [30] that realize the same effective parameters P_1 used in Fig. 2. We call these parameters P'_1 as detailed in Table I of Methods. If we consider $M = 7$, the topological JTWP can sustain $|\alpha|^2 = 164$ photons and avoids the saturation regime up to $N = 10$ sites [cf. dashed line in Fig. 3(a)]. As shown in Fig. 3(b)-(c) (dashed lines), having just two more sites compared to P_1 boosts the gain to $\mathcal{G}_N \sim 25$ dB at the center frequency, the reverse gain to -28 dB, and the noise

asymmetry to -30 dB, while keeping the same near-quantum limited added noise. Importantly, this also improves the bandwidth since the directional amplifier now provides more than 20 dB of gain over $\Delta\omega_{20} \sim 1.7J \sim 2\pi \cdot 265$ MHz.

Reaching a bandwidth on the order of GHz, requires increasing the effective hopping $J = J_a + 2g_c$ of the device. Unfortunately $g_c = K_c|\alpha|^2$ is limited by the low flux condition and cannot be increased with M [39], but we can increase J via J_a at the expense of reducing the ratio g_c/J . In particular, we consider parameters P_2 with $g_c/J = 0.25$ and $\kappa/J = 0.9$, which lies within the stable topological region as shown in Fig. 2(d). At this working point, the inverse localization length reads $\text{Re}[\zeta] \sim 0.1$, which is around half than for P_1 . This slows down the exponential growth of the gain, but an excellent performance can still be obtained with a slightly larger N since $\mathcal{G}_N \propto e^{2N\text{Re}[\zeta]}$. Using realistic circuit parameters similar to Ref. [30] (see Table I of Methods), we show in Fig. 3(d) (dashed line) that the device at P_2 can safely avoid saturation up to $N = 27$ sites, with $M = 33$ and an input flux of $|\alpha_s|^2/2\pi \sim 19$ MHz. Since $J/2\pi = 375$ MHz the topological amplifier now provides more than 20 dB of gain over a bandwidth of $\Delta\omega_{20} \approx 2.7J \approx 2\pi \cdot 1.01$ GHz, reaching a maximum of $\mathcal{G}_N = 32$ dB at the center [cf. Fig. 3(e), blue solid line]. Due to the smaller $\text{Re}[\zeta]$, the added noise has slightly increased compared to P_1 , but over the whole bandwidth $\Delta\omega_{20}$ it is still below 2.7 photons above the quantum limit (and 0.9 at the center) [cf. Fig. 3(e), red solid line]. Regarding directionality, reverse gain is below -29 dB, and noise asymmetry stays nearly flat at -40 dB [cf. Fig. 3(f), solid lines].

We see that for parameters of type P_2 , the topological JTWPAs becomes a truly broadband and directional amplifier for microwave signals. Achieving this outstanding numbers requires building a superconducting chip with a total of $N_{JJ} = (2N + 1)M = 1760$ JJs, which is less than what has been utilized in non-directional JTWPA's [8, 11]. Also note that the case $N = 2$ and $M = 30$ was experimentally implemented in Ref. [30], but without cross-Kerr coupling and therefore the device was operated as a JPA.

The topological JTWPAs is very versatile and it can also be used as an ultra-low noise directional amplifier at the expense of losing bandwidth. This requires $\text{Re}[\zeta] \gg 1$, since then the added noise becomes exponentially close to the quantum limit: $n_N^{\text{add}}(\omega) \approx 1 + e^{-2\text{Re}[\zeta(\omega)]}$. For this we consider the last operation point P_3 , for which $\text{Re}[\zeta] \sim 1$ as indicated in Fig. 2(d). The dashed lines of Figs. 3(d)-(f) display all the corresponding figures of merit. Due to extreme localization of the edge states, we see that a device with only $N = 4$ and $M = 22$ already reaches the same degree of saturation as P_2 with $N = 27$. Remarkably, near the pump frequency $\omega \sim 0$, the gain can reach 40 dB with only 0.06 photons above the quantum limit. This great performance can be maintained over a bandwidth of $\Delta\omega_{20} \sim 2J \sim 2\pi \cdot 200$ MHz with gains above 20 dB and added noise below 1.4. Reducing the noise further requires to be closer to the instability region, but operating the device gets increasingly difficult. Reverse gain is maximum -10 dB which is worse than the other cases due to

the smallness of the device with $N = 4$. Increasing N is possible but requires a large M to reduce saturation.

Throughout the performance analysis, we have considered input signals with moderate intensity $|\alpha_s|^2/2\pi < 20$ MHz in order to safely neglect saturation effects, but it is possible to increase the input power much further. We estimate that reaching $|\alpha_s|^2/2\pi \sim 320$ MHz or 2000 photons per μs (as reported for a JPA [30]) requires a topological amplifier with $M \sim 45$ when operating at the optimal point before saturation $\langle \delta a_N^\dagger(t) \delta a_N(t) \rangle \lesssim |\alpha|^2$. These are still less JJs per site than the JPA with $M = 80$ that was recently realized [37]. However, making a precise estimation of the dynamic range requires modeling the non-linear processes present in the device [12, 37], and this is left for future work. In addition, we note that the pump frequency ω_b sets the central frequency of the amplifier's response in Figs. 3 and this has been assumed fixed. By replacing all JJs in the setup by SQUIDS [12, 37], the topological JTWPAs becomes flux-tunable and it can amplify signals in the whole GHz range.

TOPOLOGICAL PROTECTION AGAINST DISORDER

The last remarkable property of the topological JTWPAs is the robustness to disorder, which can highly facilitate its experimental realization with current superconducting circuit technology. The origin of the topological protection lies in the presence of an intrinsic chiral symmetry of the extended Hamiltonian $\mathcal{H}(\omega)$ in Eq. (7), and in the robustness of the breaking of TRS via $\phi = \pi/2 \neq 0$. Smooth changes due to disorder cannot modify the symmetry class of the edge states of $\mathcal{H}(\omega)$, and the topological steady-state phase persists as long as the disorder strength is smaller than the gap, $\delta x \ll \Delta_{\text{top}}$ [25, 27, 40]. Here, δx denotes the standard deviation of any system quantity x , assumed to be normally distributed around the mean values discussed in previous sections. Note that for robust breaking of TRS we also require that the disorder in the phase fulfills $\delta\phi \ll \phi$.

Fig. 4(a) displays the topological gap Δ_{top}/J for the same topological phase shown in Fig. 2(d). We see that the gap grows with g_c/J and decreases towards the border of the phase [41]. Therefore, topological protection is optimal at the middle of the topological phase, where the gap is large $\Delta_{\text{top}}/J > 0.3J$ and the steady-state is far from the instability region. Here is where we have placed the three operation points P_1 - P_3 [cf. 4(a)]. In the following we demonstrate the robustness of the topological JTWPAs at P_1' . The behaviour for P_2 is similar and for P_3 is slightly less robust due the larger $\text{Re}[\zeta]$ (see SM).

In Figs. 4(b)-(c) we show the average gain $\bar{\mathcal{G}}_N$, reverse gain $\bar{\mathcal{G}}_N^{(R)}$, topological bandwidth $\bar{\omega}_{\text{top}}$, and added noise \bar{n}_N^{add} as function of the dimensionless disorder strength $\sigma = \delta x/J$ for all effective system parameters $x = \Delta$ (blue), $x = \kappa$ (red), $x = J$ (yellow), $x = g_s$ (purple), and $x = g_c$ (green), as well as for the phase $\sigma = \delta\phi/\phi$ (cyan). The frequency of the input signal is set to $\omega_s = -0.5J$. We see that for $\sigma \lesssim 5\%$, none of

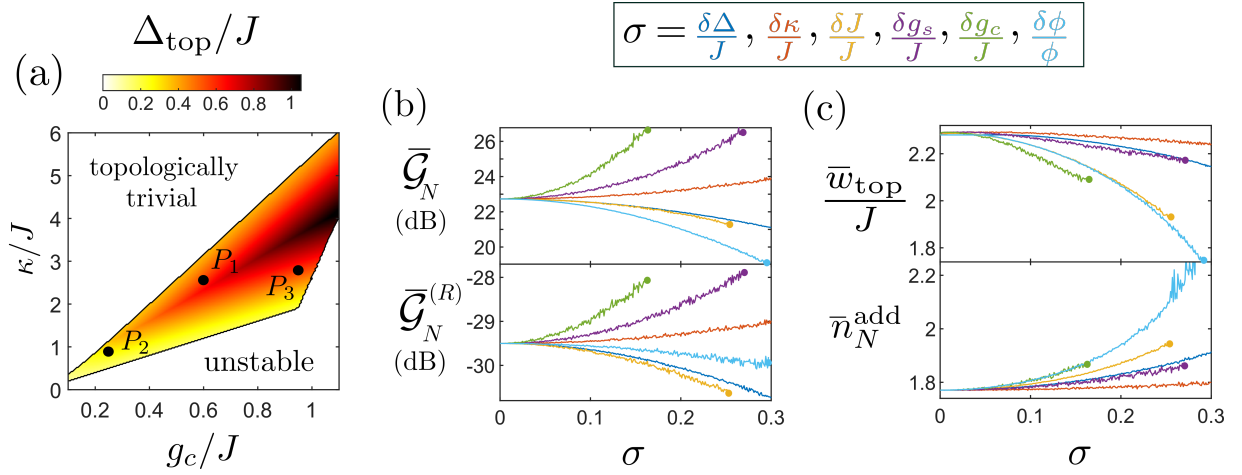


FIG. 4. **Robustness against disorder in all system parameters.** (a) Topological gap Δ_{top}/J as function of κ/J and g_c/J for the same parameters and same stable topological region as in Fig. 2(d). The black dots indicate the position of the three operation points discussed in this work. (b)-(c) Average gain \bar{G}_N , reverse gain $\bar{G}_N^{(R)}$, topological bandwidth \bar{w}_{top}/J , and added noise \bar{n}_N^{add} as function of the dimensionless disorder strength σ , defined for each system parameter as $\sigma = \delta\Delta/J$ (blue), $\sigma = \delta\kappa/J$ (red), $\sigma = \delta J/J$ (yellow), $\sigma = \delta g_s/J$ (purple), $\sigma = \delta g_c/J$ (green), and $\sigma = \delta\phi/\phi$ (cyan). All quantities are averaged over 3000 realizations for each type of disorder around the mean values defined by parameters P'_1 (corresponding to P_1 with $N = 10$, see Table I). The signal frequency is set to $\omega_s = -0.5J$. Colored dots at the end of curves indicate the disorder σ from which the steady-state becomes unstable.

the figures of merit are appreciably affected. For a larger disorder between $\sim 5\%$ and $\sim 30\%$ the topological amplification is preserved but its performance is modified. The amplifier's noise \bar{n}_N^{add} slightly increases and the topological bandwidth \bar{w}_{top} shrinks. However, some types of disorder such as $\delta g_{c,s}$ and $\delta\kappa$ can enhance the gain \bar{G}_N at the expense of reducing directionality in $\bar{G}_N^{(R)}$. This noise-induced effect is reminiscent to topological Anderson insulators observed in photonic systems [42], where noise re-normalizes the system parameters and can even trigger topological phase transitions. For even larger disorder $\sigma \simeq 1$, the gain always reduces and directional topological amplification is lost (see SM).

In addition, disorder can destabilize the amplifying steady-state depending on the operation point and/or disorder type. For P'_1 , the early termination of certain curves in Figs. 4(b)-(c) indicates the specific disorder strength at which the system becomes unstable. Including this stability analysis, we predict an overall tolerance to disorder of at least $\sigma \lesssim 10\%$ in all system parameters, while retaining the excellent performance of the directional amplification. A practical implementation of the topological JTWPA will be mainly affected by disorder and inhomogeneities inherent to the fabrication of JJs [29] and this constitutes a natural protection against it.

PROSPECTS

We have presented the design of a quantum amplifier of weak microwave signals that works in a broadband, quantum-limited and directional regime by exploiting non-Hermitian topological effects. Our work opens several routes for exploring further technological applications, as well as fundamen-

tal physics of topologically driven-dissipative systems. The topological JTWPA device can be fully integrated on-chip and be used as compact broadband pre-amplifier without isolators, which can help scaling up quantum computing and quantum sensing devices [14]. Our quantum amplifier could also be applied for broadband detection of single-photons [43]. Further work will be devoted to the study of the properties and efficiency of such single-photon detector. Saturation effects induced by Kerr non-linearities can lead to novel regimes of operation of our device [12], which can be theoretically addressed by approximations like mean-field or Matrix Product State techniques.

From a more fundamental perspective, our proposal is also a versatile platform for the quantum simulation of open quantum systems [32, 44], non-Hermitian physics [45, 46], and novel topological driven-dissipative phases of matter [47, 48], including those with disorder [49] and strong photon-photon interactions [50, 51]. For quantum simulation, a particularly convenient aspect of our design is that the strength of the synthetic gauge field and the nonlinear interactions can be conveniently controlled via the external pump, without requiring Floquet engineering [28] or external magnetic fields.

METHODS

Superconducting circuit model

We provide the detailed superconducting circuit design to implement the topological JTWPA, as well as the connection between the effective model of the main text and the microscopic circuit quantities. As shown in Fig. 5(a), at each node j

of the circuit we define a flux variable $\phi_j^\mu(t)$, with index $\mu = a$ corresponding to the JJ array and $\mu = b$ to the auxiliary linear array. These fluxes couple via Josephson junctions and capacitances and their dynamics is governed by the Langrangian $L = L_{\text{JJA}} + L_{\text{aux}}$, where

$$L_{\text{JJA}} = \sum_j \frac{C_a}{2} (\dot{\phi}_j^a)^2 + \frac{C'_a}{2} \sum_j (\dot{\phi}_{j+1}^a - \dot{\phi}_j^a)^2 \quad (10)$$

$$+ E_J \sum_j \cos\left(\frac{\phi_j^a}{\Phi_0}\right) + E'_J \sum_j \cos\left(\frac{\phi_{j+1}^a - \phi_j^a}{\Phi_0}\right),$$

$$L_{\text{aux}} = \sum_j \frac{C_b}{2} (\dot{\phi}_j^b)^2 - \sum_j \frac{(\phi_j^b)^2}{2L_b} + \frac{C'_b}{2} \sum_j (\dot{\phi}_{j+1}^b - \dot{\phi}_j^b)^2, \quad (11)$$

$$+ \sum_j \frac{C_{ab}}{2} (\dot{\phi}_j^b - \dot{\phi}_j^a)^2.$$

Regarding the JJ array, we consider on-site and inter-site capacitances denoted by C_a and C'_a , respectively, as well as on-site and inter-site Josephson junctions, which induce nonlinear potentials with Josephson energies E_J and E'_J , respectively. In addition, $\Phi_0 = \hbar/(2e)$ denotes the reduced flux quantum. In the auxiliary chain, superconducting linear resonators are realized at each node j by LC circuits with capacitance C_b and inductance L_b . These resonators are coupled via inter-site capacitances C'_b and also couple to the JJ array via an inter-array capacitance C_{ab} . The left- and right-most sites of the array are coupled to ground which provides the boundary conditions, $\phi_0^\mu = \phi_{N+1}^\mu = 0$.

We consider the low flux regime, $|\phi_j^a| \ll \Phi_0$, so that the nonlinear JJ potentials can be expanded as $\cos(x) = 1 - x^2/2 + x^4/24 + \mathcal{O}(x^6)$, and the JJ array behaves as a weakly anharmonic resonator array with self- and cross-Kerr couplings coming from the fourth order terms $\sim (\phi_j^a)^4$ and $\sim (\phi_{j+1}^a - \phi_j^a)^4$. Following the canonical quantization procedure [4, 51], we can express the flux ϕ_j^μ and charge $q_j^\mu = \partial L / \partial \dot{\phi}_j^\mu$ variables in terms localized bosonic modes a_j and b_j , for the JJ and auxiliary arrays, respectively. The coherent dynamics of these modes is described by the total Hamiltonian, $H = H_{\text{JJA}} + H'_{\text{JJA}} + H_{\text{aux}}$, with H_{JJA} and H_{aux} given in Eqs. (1)-(2), and $H'_{\text{JJA}} = \frac{K_c}{4} \sum_j [2(a_j^\dagger)^2 a_j a_{j+1} + 2a_j^\dagger a_{j+1}^\dagger (a_{j+1})^2 - (a_j^\dagger)^2 (a_{j+1})^2 + \text{h.c.}]$. This extra Hamiltonian term H'_{JJA} does not qualitatively change the dynamics of the JJ array, but it must be included to obtain the proper parametric amplifier Hamiltonian in Eq. (4).

Regarding the effective parameters of the model, the on-site frequency of the JJ array modes reads $\omega_a = (L_a^{\text{eq}} C_a^{\text{eq}})^{-1/2}$, with $C_a^{\text{eq}} = C_a + 2C'_a + C_{ab}$ the equivalent capacitance and $L_a^{\text{eq}} = (L'_J L_J) / (L'_J + 2L_J)$ the equivalent inductance. Here, $L_J = \Phi_0^2 / E_J$ and $L'_J = \Phi_0^2 / E'_J$ are the on-site and inter-site Josephson inductances, respectively. In addition, the linear hopping in the JJ array contains capacitive and inductive contributions $J_a = \frac{\omega_a}{2} (C'_a / C_a^{\text{eq}} - L_a^{\text{eq}} / L'_J)$, whereas the self- and cross-Kerr coupling strengths read $K_s = E_C / \hbar$ and $K_c = 2(E_C / \hbar) (L_a^{\text{eq}} / L'_a)$, with $E_C = e^2 / (2C_a^{\text{eq}})$ the charg-

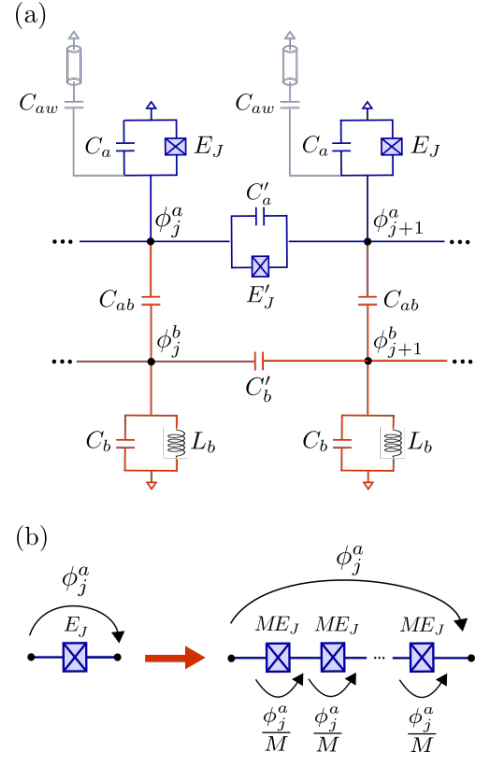


FIG. 5. **Detailed circuit diagram for two adjacent sites of the topological JTWP.** (a) Flux variables ϕ_j^μ are defined at each node of the circuit given by the chain index $\mu = a, b$ and the position j . The JJ array (blue) is composed of on-site and inter-site JJs with Josephson energies E_J and E'_J , as well as capacitances C_a and C'_a . Each site of the JJ array is additionally coupled to a 50Ω transmission line with capacitance C_{aw} (grey). Finally, the JJ array also couples via a capacitance C_{ab} to a linear array of superconducting resonators (red), given by LC circuits with on-site capacitance C_b and inductance L_b . These resonators are also coupled by inter-site capacitances C'_b . (b) Optional upgrade for the topological JTWP to increase its dynamic range. It consists in replacing all intra- and inter-site JJs in the array (a) by a sub-array of M JJs in series. Increasing $E_J, E'_J \rightarrow ME_J, ME'_J$ reduces the flux drop along each JJ by a factor M , and thereby increases by a factor M^2 the photons that the system can sustain before saturation [12, 30].

ing energy. Regarding the auxiliary chain, the on-site frequency reads $\omega_b = (L_b C_b^{\text{eq}})^{-1/2}$, with $C_b^{\text{eq}} = C_b + 2C'_b + C_{ab}$ its equivalent capacitance. The intra-array and inter-array linear hoppings are purely capacitive and take the form $J_b = \frac{\omega_b}{2} (C'_b / C_b^{\text{eq}})$ and $J_{ab} = \frac{\sqrt{\omega_a \omega_b}}{2} C_{ab} (C_a^{\text{eq}} C_b^{\text{eq}})^{-1/2}$, respectively. We note to derive H , we neglect long-range capacitive couplings provided $C'_a, C_{ab} \ll C_a^{\text{eq}}$ and $C'_b, C_{ab} \ll C_b^{\text{eq}}$, and we apply the rotating wave approximation, provided all couplings are much smaller than the on-site frequencies ω_a and ω_b . Note that Kerr-couplings induce small shifts $\omega_a \rightarrow \omega_a - K_c - K_s$ and $J_a \rightarrow J_a + K_c$. Finally, the low flux approximation does not only require $E_C \ll E_J, E'_J$ as for transmons [4]. As shown in Ref. [12], we also require that the mean number of excitations on each site is bounded as $|\alpha_j|^2 \ll (\Phi_0 / 2\phi_{\text{zpf}})^2$, with $\phi_{\text{zpf}} = \sqrt{\hbar / (2C_a^{\text{eq}} \omega_a)}$ the zero

flux fluctuation of the JJ array. This limits the dynamic range of the device, but as demonstrated in Refs. [12, 30, 37], we can replace each JJ in the setup by a sub-array of M JJs in series to increase the upper bound by a factor M^2 . This requires increasing the Josephson energies as $E_J, E'_J \rightarrow ME_J, ME'_J$ such that the phase drop on each intra- and inter-site JJ reduces by a factor M [cf. Fig. 5(b)]. Notice, however, that the total phase drop along each sub-array remains the same and therefore all linear circuit parameters are unchanged except for the Kerr non-linearities, which reduce as $K_c, K_s \rightarrow K_c/M^2, K_s/M^2$ [12].

Coupling to input/output ports, dissipation, and driving

Input/output ports are realized by standard transmission lines with $Z_0 = 50\Omega$ impedance. As shown in Figs. 1(a) and 5(a), we couple one of these lines to each site of the JJ array with capacitance C_{aw} , as well as to the boundaries of the auxiliary array, $j = 1$ and $j = N$, with a different capacitance C_{bw} . Assuming a Markovian coupling, the local decay rate induced on each site of the JJ array is given by $\kappa = (C_{wa}/C_a^{\text{eq}})^2(Z_0/Z_a)(\omega_a/2)$ [4, 44], with $Z_a = \sqrt{L_a^{\text{eq}}/C_a^{\text{eq}}}$ the impedance of the JJ array. Similarly, the decay rate induced on the boundaries of the auxiliary chain reads $\Gamma = (C_{wb}/C_b^{\text{eq}})^2(Z_0/Z_b)(\omega_b/2)$, with $Z_b = \sqrt{L_b^{\text{eq}}/C_b^{\text{eq}}}$. Notice that the coupling to the transmission lines renormalizes the equivalent capacitances of the JJ array as $C_a^{\text{eq}} \rightarrow C_a^{\text{eq}} + C_{aw}$. For the auxiliary chain, this change is compensated by choosing a slightly lower capacitance $C_b \rightarrow C_b - C_{bw}$ only at the boundaries, $j = 1$ and $j = N$.

In addition, we use the input port on the first auxiliary site $j = 1$ to perform a strong and resonant coherent drive only on mode b_1 . This is described by Hamiltonian $H_b^{(p)} = 2i\Omega_b \cos(\omega_b t)(b_1 + b_1^\dagger)$, with $\Omega_b = (C_{wb}/2C_b^{\text{eq}})\sqrt{Z_0/Z_b}\sqrt{P_b/\hbar}$ the driving strength and P_b the pump power [4].

Four-wave mixing via auxiliary array and perfect phase matching

The complete driven-dissipative dynamics of the two coupled arrays is given by the quantum Langevin equations,

$$\dot{a}_j = i[H', a_j] - \frac{\kappa}{2}a_j - \sqrt{\kappa}a_j^{\text{in}}(t), \quad (12)$$

$$\dot{b}_j = i[H', b_j] - \left(\frac{\Gamma}{2}b_j + \sqrt{\Gamma}b_j^{\text{in}}(t)\right)(\delta_{j1} + \delta_{jN}), \quad (13)$$

where $H' = H + H_b^{(p)}$ contains all coherent couplings and the driving on the first site of the auxiliary array. In addition, $a_j^{\text{in}}(t)$ and $b_j^{\text{in}}(t)$ describe the vacuum input fields at site j of the JJ and auxiliary arrays, respectively. For a strong pump, we can do four-wave-mixing and displace all coupled modes as $a_j(t) = (\alpha + \delta a_j(t))e^{-i(\phi_j + \omega_b t)}$ and

$b_j = (\beta_j + \delta b_j(t))e^{-i\omega_b t}$, where δa_j and δb_j are quantum fluctuations around the large mean displacements α and β_j , respectively. Using the previous ansatz in Eqs. (12)-(13), we find classical coupled equations for the mean displacements,

$$\dot{\alpha} = -\left(\frac{\kappa}{2} - i(A + B|\alpha|^2)\right)\alpha - iJ_{ab}\beta_j e^{i\phi_j}, \quad (14)$$

$$\dot{\beta}_j = -\sum_l \mathcal{I}_{jl}\beta_l + \Omega_b(1 + e^{2i\omega_b t})\delta_{j1} - iJ_{ab}\alpha e^{-i\phi_j}, \quad (15)$$

where $A = \omega_b - \omega_a - 2J_a \cos(\phi)$, $B = K_s + K_c[2 + \cos(2\phi) - 4\cos(\phi)]$, and \mathcal{I}_{jl} are matrix elements given by $\mathcal{I}_{jl} = \frac{\Gamma}{2}\delta_{jl}(\delta_{j1} + \delta_{jN}) + iJ_b(\delta_{l,j+1} + \delta_{l,j-1})$. Notice that we have assumed an homogeneous mean displacement α for the JJ array, which can only be a valid solution if $\beta_j \sim e^{-i\phi_j}$ and thereby cancels the j -dependence in the last term in Eq. (14). Here, we show that this is indeed the case for the steady-state of the system if $\Gamma = 2J_b$ because this realizes perfect impedance matching at the boundaries of the auxiliary chain. In particular, when $\Gamma = 2J_b$, the matrix \mathcal{I}_{jl} can be inverted exactly as $[\mathcal{I}^{-1}]_{jl} = e^{-i(\pi/2)|j-l|}/(2J_b)$ [52], and therefore we can solve for the steady-state solution ($t \rightarrow \infty$) of Eq. (15) as,

$$\beta_j = \frac{i\Omega_b}{2J_b}e^{-i(\pi/2)j} - i\frac{J_{ab}}{2J_b}\alpha \sum_l e^{-i(\phi_l + \pi/2|j-l|)}. \quad (16)$$

Note that we have neglected fast oscillations due to the non-RWA driving term $\sim e^{2i\omega_b t}$ in Eq. (15), provided $J_b, J_{ab} \ll \omega_b \lesssim \Omega_b$. Replacing Eq. (16) in (14), we see that β_j induces an effective driving with strength $\Omega_a = (J_{ab}/2J_b)\Omega_b$ on the JJ array, and its phase $\phi = \pi/2$ provides perfect phase matching. As a result, the steady state displacement α satisfies a nonlinear Duffing oscillator equation [12, 37],

$$(\kappa/2 - i[\omega_b - \omega_a + (K_c + K_s)|\alpha|^2])\alpha = \Omega_a, \quad (17)$$

provided we neglect non-local dissipative processes originated by the second term of the auxiliary displacement in Eq. (16). This is justified when the associated decay rate $\kappa_{\text{nl}} = J_{ab}^2/(2J_b)$ is much smaller than all other effective quantities $\Omega_a, \kappa, |\omega_b - \omega_a|, K_s|\alpha|^2, K_c|\alpha|^2$. Notice that the presence of additional local decay on the auxiliary cavities b_j deteriorates the perfect absorbing condition, but the topological steady state phase is robust as long as this unwanted decay is much smaller than J_b .

Regarding the dynamics of the quantum fluctuations δa_j and δb_j , we see that they decouple when being far detuned, $J_{ab}, J_b \ll |\omega_b - \omega_a|$. Under these conditions and assuming a strong displacement $|\alpha|^2 \gg \langle \delta a_j^\dagger \delta a_j \rangle$, it is possible to derive an effective linear dynamics for the fluctuations $\delta a_j(t)$ of the JJ array as

$$\delta \dot{a}_j = i[H_{\text{pa}}, \delta a_j] - \frac{\kappa}{2}\delta a_j - \sqrt{\kappa}a_j^{\text{in}}(t) + \mathcal{O}(|\alpha|\delta a_j^3), \quad (18)$$

where H_{pa} is the topological parametric amplifier Hamiltonian given in Eq. (4) with effective quantities $J = J_a + 2K_c|\alpha|^2$, $g_c = K_c|\alpha|^2$, and $g_s = (K_c - K_s)|\alpha|^2$. The non-linear interactions of order $\sim |\alpha|\delta a_j^3$ or higher are responsible for saturation effects in the amplifier and therefore $|\alpha|^2$ should be as large as possible, only limited by the low flux condition.

	N	M	N_{JJ}	g_c/J	κ/J	C_a (fF)	C'_a (fF)	ME_J/h (THz)	C_{aw} (fF)	C_{ab} (fF)	C_a^{eq} (fF)	L_a^{eq} (nH)	Z_a (Ω)	E_C/h (MHz)	$K_c/2\pi$ (kHz)	$J_a/2\pi$ (MHz)	$\kappa/2\pi$ (MHz)	P_b (dBm)	$ \alpha ^2$	$J/2\pi$ (MHz)
P_1	8	1	17	0.6	2.6	1800	1030	1.01	387	1.58	4240	0.08	4.4	4.6	2270	-31	406	-68.8	41	156
P'_1	10	7	147	0.6	2.6	66.8	83.5	0.57	110	0.45	344	1.00	54	56	572	-31	406	-62.8	164	156
P_2	27	32	1760	0.25	0.9	41.3	101	2.62	100	0.46	345	1.00	54	56	27	188	338	-50.3	3430	375
P_3	4	22	198	0.95	2.8	95.3	79.0	1.80	91	0.45	345	1.00	54	56	58	-89	276	-53.7	1621	99

TABLE I. **Circuit parameters for various operation points of the topological JTWP.** The first five columns show general quantities that describe each operation point P_1 , P'_1 , P_2 , and P_3 , of the amplifier, namely the number of sites N of the JJ array, number of JJs M on each sub-array, total number of JJs N_{JJ} in the device, ratio between non-local parametric drive and hopping g_c/J , ratio between local decay and hopping κ/J . The next eight columns show specific circuit parameters of the JJ array, such as on-site capacitance C_a , inter-site capacitance C'_a , Josephson frequency of each on-site JJ ME_J/h (inter-site Josephson frequency is always half), capacitance C_{aw} of the coupling to the input/output ports, capacitance C_{ab} of the coupling to the auxiliary array, equivalent (total) on-site capacitance C_a^{eq} , equivalent on-site inductance L_a^{eq} , and impedance Z_a . The next four columns show effective properties of the JJ array such charging frequency E_C/h , cross-Kerr nonlinearity K_c (self-Kerr is always twice), linear hopping J_a , and effective decay rate κ for coupling the input/output ports. The last three columns show the power P_b of the pump on the auxiliary array, the mean number of photons $|\alpha|^2$ that this pump induces on the JJ array, and the effective inter-site hopping $J = J_a + 2K_c|\alpha|^2$ which ultimately determines the bandwidth of the topological JTWP.

Analytical solution for mean photon displacement

The third-order non-linear equation (17) for the mean steady-state displacement $|\alpha|^2$ admits analytical solutions. In particular, for $\Delta = 0$ as it is of interest in this work, we have that $|\alpha|^2 = [\kappa/(K_s + K_c)]n$ and $\omega_b - \omega_a = -2\kappa n$, where n is a real solution of the third order equation, $n^3 + n/4 = \xi$, which reads

$$n(\xi) = \frac{3^{1/3}(36\xi + \sqrt{3 + 1296\xi^2})^{2/3} - 3^{2/3}}{6(36\xi + \sqrt{3 + 1296\xi^2})^{1/3}}. \quad (19)$$

Here, the dimensionless parameter $\xi = (|\Omega_a|/\kappa)^2[(K_s + K_c)/\kappa]$ controls the size of n , specially via the pump power P_b on the auxiliary array which determines the effective driving strength on the JJ array, $\Omega_a = (J_{ab}/J_b)(C_{wb}/2C_b^{\text{eq}})\sqrt{Z_0/Z_b}\sqrt{P_b/\hbar}$. In contrast to a single-site JPA [12], the topological JTWP has no instability at $\xi > 1/\sqrt{27}$ and it can go much further in n , as long as the combination of the effective quantities in Eqs. (5)-(6) give a stable steady-state. This is because the equation for the fluctuations of the topological JTWP is different than for a JPA, although the nonlinear equation for the mean-field displacement $|\alpha|^2$ is the same.

Experimental parameters

In our work we analyze three operation points $P_1 - P_3$ for the topological JTWP [cf. Fig. 2(d)]. For P_1 we consider a parameters similar to Ref. [31] such that the JJ array has a capacitance $C_a^{\text{eq}} \sim 4$ pF, Josephson inductance $L_a^{\text{eq}} \sim 0.08$ nH, and impedance $Z_a \sim 4.4 \Omega$. For P'_1 , P_2 , and P_3 , we consider parameters similar to Ref. [30] with $C_a^{\text{eq}} \sim 0.34$ pF, $L_a^{\text{eq}} \sim 1$ nH, and $Z_a \sim 54 \Omega$. In all cases, the on-site frequency is fixed to $\omega_a/2\pi \sim 8.57$ GHz, the non-local parametric drive $g_c/2\pi = 94$ MHz, and the ratio $g_s/g_c = 1$. This latter condition requires $K_s/K_c = 2$ which is controlled by

setting $E_J/E'_J = 2$. Strength of Kerr nonlinearities depend on M and on the charging energy E_C . These and other effective quantities of the JJ array are indicated in Table I for each operation point.

The parameters of the auxiliary array and its input/output ports are fixed for all operation points to $L_b = 0.992$ nH, $C_b = 397$ fF, $C'_b = 0.5$ fF, $C_{bw} = 19.9$ fF, $Z_b = 50\Omega$, and $Z_w = 50\Omega$. This leads to a frequency $\omega_b/2\pi = 8$ GHz, intra-array hopping $J_b/2\pi = 5$ MHz, intra-array hopping $J_{ab}/2\pi = 5$ MHz, and decay rate on the boundaries $\Gamma/2\pi = 10$ MHz ($= 2J_b$). Importantly, for these parameters the effective detuning on the JJ array vanishes $\Delta = 0$, the non-local decay on the JJ array $\kappa_{nl}/2\pi = 2.5$ MHz can be neglected compared to all other effective quantities, and the intra-array detuning $|\omega_b - \omega_a|/2\pi = 570$ MHz is much larger than J_{ab} and J_b , which leads to $\phi = \pi/2$. Note that we have neglected intrinsic decay of auxiliary cavities provided they are smaller than κ_{nl} . Finally, the pump and signal powers, depend strongly on the operation point of the amplifier and its saturation properties. In particular, we consider $|\alpha_s|^2/2\pi \sim 5$ MHz for P_1 , P'_1 , and P_3 , whereas for P_2 we have $|\alpha_s|^2/2\pi \sim 19$ MHz. The pump powers P_b are chosen in the range between -70 to -50 dBm [cf. Table I], which is standard in JTWPs [14].

ACKNOWLEDGMENTS

This work has been supported by funding from Spanish project PGC2018-094792-B-I00 (MCIU/AEI/FEDER, UE), CSIC Research Platform on Quantum Technologies PTI-001, and Proyecto Sinergico CAM 2020 Y2020/TCS-6545 (NanoQuCo-CM). T.R. further acknowledges support from the Juan de la Cierva fellowship IJC2019-040260-I.

* t.amos.delrio@gmail.com

† diego.porras@csic.es

- [1] D. M. P. Smith, L. Bakker, R. H. Witvers, B. E. M. Woestenburg, and K. D. Palmer, *International Journal of Microwave and Wireless Technologies* **5**, 453 (2013).
- [2] A. N. Cleland, J. S. Aldridge, D. C. Driscoll, and A. C. Gossard, *Appl. Phys. Lett.* **81**, 1699 (2002).
- [3] A. Blais, A. L. Grimsmo, S. Girvin, and A. Wallraff, *Rev. Mod. Phys.* **93**, 025005 (2021).
- [4] J. J. García-Ripoll, *Quantum Information and Quantum Optics with Superconducting Circuits* (Cambridge University Press, Cambridge, 2022).
- [5] R. Vijay, D. H. Slichter, and I. Siddiqi, *Phys. Rev. Lett.* **106**, 110502 (2011).
- [6] T. Walter, P. Kurpiers, S. Gasparinetti, P. Magnard, A. Potočník, Y. Salathé, M. Pechal, M. Mondal, M. Oppliger, C. Eichler, and A. Wallraff, *Phys. Rev. Applied* **7**, 054020 (2017).
- [7] R. Dassonneville, T. Ramos, V. Milchakov, L. Planat, E. Dumur, F. Foroughi, J. Puertas, S. Leger, K. Bharadwaj, J. Delaforce, C. Naud, W. Hasch-Guichard, J. García-Ripoll, N. Roch, and O. Buisson, *Phys. Rev. X* **10**, 011045 (2020).
- [8] C. Macklin, K. O'Brien, D. Hover, M. E. Schwartz, V. Bolkhovskiy, X. Zhang, W. D. Oliver, and I. Siddiqi, *Science* **350**, 307 (2015).
- [9] T. C. White, J. Y. Mutus, I.-C. Hoi, R. Barends, B. Campbell, Y. Chen, Z. Chen, B. Chiaro, A. Dunsworth, E. Jeffrey, J. Kelly, A. Megrant, C. Neill, P. J. J. O'Malley, P. Roushan, D. Sank, A. Vainsencher, J. Wenner, S. Chaudhuri, J. Gao, and J. M. Martinis, *Appl. Phys. Lett.* **106**, 242601 (2015).
- [10] L. Planat, A. Ranadive, R. Dassonneville, J. Puertas Martínez, S. Léger, C. Naud, O. Buisson, W. Hasch-Guichard, D. M. Basko, and N. Roch, *Phys. Rev. X* **10**, 021021 (2020).
- [11] P. Winkel, I. Takmakov, D. Rieger, L. Planat, W. Hasch-Guichard, L. Grünhaupt, N. Maleeva, F. Foroughi, F. Henriques, K. Borisov, J. Ferrero, A. V. Ustinov, W. Wernsdorfer, N. Roch, and I. M. Pop, *Phys. Rev. Applied* **13**, 024015 (2020).
- [12] C. Eichler and A. Wallraff, *EPJ Quantum Technol.* **1**, 2 (2014).
- [13] A. Roy and M. Devoret, *Comptes Rendus Physique Quantum microwaves / Micro-ondes quantiques*, **17**, 740 (2016).
- [14] M. Esposito, A. Ranadive, L. Planat, and N. Roch, *Appl. Phys. Lett.* **119**, 120501 (2021).
- [15] B. Abdo, K. Sliwa, L. Frunzio, and M. Devoret, *Phys. Rev. X* **3**, 031001 (2013).
- [16] K. Sliwa, M. Hatridge, A. Narla, S. Shankar, L. Frunzio, R. Schoelkopf, and M. Devoret, *Phys. Rev. X* **5**, 041020 (2015).
- [17] A. Metelmann and A. Clerk, *Phys. Rev. X* **5**, 021025 (2015).
- [18] F. Lecocq, L. Ranzani, G. Peterson, K. Cicak, R. Simmonds, J. Teufel, and J. Aumentado, *Phys. Rev. Applied* **7**, 024028 (2017).
- [19] K. Fang, J. Luo, A. Metelmann, M. H. Matheny, F. Marquardt, A. A. Clerk, and O. Painter, *Nature Phys* **13**, 465 (2017).
- [20] S. Pucher, C. Liedl, S. Jin, A. Rauschenbeutel, and P. Schneeweiss, *Nat. Photon.* **16**, 380 (2022).
- [21] J. Heinsoo, C. K. Andersen, A. Remm, S. Krinner, T. Walter, Y. Salathé, S. Gasparinetti, J.-C. Besse, A. Potočník, A. Wallraff, and C. Eichler, *Phys. Rev. Applied* **10**, 034040 (2018).
- [22] L. Lu, J. D. Joannopoulos, and M. Soljačić, *Nature Photonics* **8**, 821 (2014), number: 11 Publisher: Nature Publishing Group.
- [23] T. Ozawa, H. M. Price, A. Amo, N. Goldman, M. Hafezi, L. Lu, M. C. Rechtsman, D. Schuster, J. Simon, O. Zilberberg, and I. Carusotto, *Rev. Mod. Phys.* **91**, 015006 (2019).
- [24] V. Peano, M. Houde, F. Marquardt, and A. A. Clerk, *Phys. Rev. X* **6**, 041026 (2016).
- [25] D. Porras and S. Fernández-Lorenzo, *Phys. Rev. Lett.* **122**, 143901 (2019).
- [26] C. C. Wanjura, M. Brunelli, and A. Nunnenkamp, *Nature Communications* **11**, 3149 (2020), number: 1 Publisher: Nature Publishing Group.
- [27] T. Ramos, J. J. García-Ripoll, and D. Porras, *Phys. Rev. A* **103**, 033513 (2021).
- [28] P. Roushan, C. Neill, A. Megrant, Y. Chen, R. Babbush, R. Barends, B. Campbell, Z. Chen, B. Chiaro, A. Dunsworth, A. Fowler, E. Jeffrey, J. Kelly, E. Lucero, J. Mutus, P. J. J. O'Malley, M. Neeley, C. Quintana, D. Sank, A. Vainsencher, J. Wenner, T. White, E. Kapit, H. Neven, and J. Martinis, *Nature Physics* **13**, 146 (2017).
- [29] J. M. Kreikebaum, K. P. O'Brien, A. Morvan, and I. Siddiqi, *Supercond. Sci. Technol.* **33**, 06LT02 (2020).
- [30] C. Eichler, Y. Salathe, J. Mlynec, S. Schmidt, and A. Wallraff, *Phys. Rev. Lett.* **113**, 110502 (2014).
- [31] J. Y. Mutus, T. C. White, R. Barends, Y. Chen, Z. Chen, B. Chiaro, A. Dunsworth, E. Jeffrey, J. Kelly, A. Megrant, C. Neill, P. J. J. O'Malley, P. Roushan, D. Sank, A. Vainsencher, J. Wenner, K. M. Sundqvist, A. N. Cleland, and J. M. Martinis, *Appl. Phys. Lett.* **104**, 263513 (2014).
- [32] M. Kounalakis, C. Dickel, A. Bruno, N. K. Langford, and G. A. Steele, *npj Quantum Inf* **4**, 38 (2018).
- [33] A. Ranadive, M. Esposito, L. Planat, E. Bonet, C. Naud, O. Buisson, W. Guichard, and N. Roch, *Nat Commun* **13**, 1737 (2022).
- [34] A. Gómez-León, T. Ramos, A. González-Tudela, and D. Porras, *Phys. Rev. A* **106**, L011501 (2022).
- [35] S. Ryu, A. P. Schnyder, A. Furusaki, and A. W. W. Ludwig, *New J. Phys.* **12**, 065010 (2010).
- [36] M. Z. Hasan and C. L. Kane, *Rev. Mod. Phys.* **82**, 3045 (2010).
- [37] L. Planat, R. Dassonneville, J. P. Martínez, F. Foroughi, O. Buisson, W. Hasch-Guichard, C. Naud, R. Vijay, K. Murch, and N. Roch, *Phys. Rev. Applied* **11**, 034014 (2019).
- [38] Notice that in the original work by Caves [53], the quantum limit of minimum noise corresponds to $n_j^{\text{add}} = 1/2$ due to a different convention in the definition of the noise power.
- [39] Using sub-arrays of M JJs [12] does not modify the linear properties of the superconducting circuit, but reduces the Kerr-nonlinearities as $K_{c,s} \rightarrow K_{c,s}/M^2$. Since $|\alpha|^2$ can be increased maximum by a factor M^2 , the effective quantities $g_c = K_c|\alpha|^2$ and $g_s = (K_s - K_c)|\alpha|^2$ are not modified.
- [40] C. C. Wanjura, M. Brunelli, and A. Nunnenkamp, *Phys. Rev. Lett.* **127**, 213601 (2021).
- [41] Due to finite size effects, Δ_{top} does not vanish at the interface with the trivial region $E_0 > 1/N$. In the thermodynamic limit $N \rightarrow \infty$, zero energy modes become exact $E_0 = 0$ and the gap vanishes exactly at the boundary.
- [42] S. Stützer, Y. Plotnik, Y. Lumer, P. Titum, N. H. Lindner, M. Segev, M. C. Rechtsman, and A. Szameit, *Nature* **560**, 461 (2018).
- [43] A. L. Grimsmo, B. Royer, J. M. Kreikebaum, Y. Ye, K. O'Brien, I. Siddiqi, and A. Blais, *Phys. Rev. Applied* **15**, 034074 (2021).
- [44] P.-O. Guimond, B. Vermersch, M. L. Juan, A. Sharafiev, G. Kirchmair, and P. Zoller, *npj Quantum Information* **6**, 1 (2020).
- [45] V. P. Flynn, E. Cobanera, and L. Viola, *Phys. Rev. Lett.* **127**, 245701 (2021).
- [46] K. Kawabata, K. Shiozaki, M. Ueda, and M. Sato, *Phys. Rev. X* **9**, 041015 (2019).

- [47] A. Gómez-León, T. Ramos, A. González-Tudela, and D. Porras, Non-Hermitian topological phases in traveling-wave parametric amplifiers, arXiv:XXXX.XXXXX (2022), submitted.
- [48] A. McDonald, R. Hanai, and A. A. Clerk, [Phys. Rev. B **105**, 064302 \(2022\)](#).
- [49] J. Tangpanitanon, V. M. Bastidas, S. Al-Assam, P. Roushan, D. Jaksch, and D. G. Angelakis, [Phys. Rev. Lett. **117**, 213603 \(2016\)](#).
- [50] M. Hafezi, M. D. Lukin, and J. M. Taylor, [New J. Phys. **15**, 063001 \(2013\)](#).
- [51] J. Jin, D. Rossini, R. Fazio, M. Leib, and M. J. Hartmann, [Phys. Rev. Lett. **110**, 163605 \(2013\)](#).
- [52] T. Ramos, B. Vermersch, P. Hauke, H. Pichler, and P. Zoller, [Phys. Rev. A **93**, 062104 \(2016\)](#).
- [53] C. M. Caves, [Phys. Rev. D **26**, 1817 \(1982\)](#).

Supplemental Material for: Directional Josephson traveling-wave parametric amplifier via non-Hermitian topology

Tomás Ramos, Álvaro Gómez-León, Juan José García-Ripoll, Alejandro González-Tudela, and Diego Porras
Institute of Fundamental Physics IFF-CSIC, Calle Serrano 113b, 28006 Madrid, Spain.

CONTENTS

- I.— Spectral properties of the amplifier from Green's functions.
- II.— Directional amplification from edge states of extended Hamiltonian.
- III.— Topological protection to disorder at operation points P_2 and P_3 .

I.— SPECTRAL PROPERTIES OF THE AMPLIFIER FROM GREEN'S FUNCTIONS

In this section, we show how to obtain all spectral properties of the amplifier such as gain, reverse gain, and noise from the information contained in the Green's function $G(\omega) = (\omega - H_{\text{nh}})^{-1}$, where H_{nh} is the non-Hermitian matrix defined in Eq. (6) of the main text. We also show that signal ($\omega = \omega_s$) and idler ($\omega = -\omega_s$) fields have the same topological amplifying properties.

The output operator $\bar{a}_j^{\text{out}}(t)$ characterizes the amplified field leaving the device at the output port j . In the rotating frame with the pump frequency ω_b , this is related to the input field by a standard input-output relation [4],

$$\bar{a}_j^{\text{out}}(t) = \bar{a}_j^{\text{in}}(t) + \sqrt{\kappa}(\alpha + \delta a_j(t))e^{-i\phi j}. \quad (20)$$

Here, $\bar{a}_j^{\text{in}}(t) = e^{-i\phi j} a_j^{\text{in}}(t)$, with $a_j^{\text{in}}(t)$ the input operator in Eq. (5).

Since the Langevin equations (5) are linear, we can solve them exactly in Fourier space. Defining the Fourier transform of the fluctuation and input operators as $\delta a_j(\omega) = (2\pi)^{-1/2} \int dt e^{i\omega t} \delta a_j(t)$ and $a_j^{\text{in}}(\omega) = (2\pi)^{-1/2} \int d\omega e^{i\omega t} \delta a_j^{\text{in}}(t)$, we have

$$\begin{aligned} \delta a_j(\omega) = & -i\sqrt{\kappa} \sum_l G_{jl}(\omega) e^{i\phi l} \bar{a}_l^{\text{in}}(\omega) \\ & -i\sqrt{\kappa} \sum_l G_{j,N+l}(\omega) e^{-i\phi l} \bar{a}_l^{\text{in}\dagger}(-\omega), \end{aligned} \quad (21)$$

where $G_{jl}(\omega)$ and $G_{j,N+l}(\omega)$ are the normal and anomalous components of the $2N \times 2N$ Green's function matrix $G(\omega) = (\omega - H_{\text{nh}})^{-1}$.

To characterize the amplifying properties of the device, we measure the output field $\bar{a}_j^{\text{out}}(t)$ at site j when sending a coherent signal of amplitude α_s and frequency ω_s at input port m (ω_s is taken with respect to the pump frequency ω_b). Including vacuum fluctuations $\delta \bar{a}_j^{\text{in}}(t)$ at all inputs j , the input

field then reads

$$\bar{a}_j^{\text{in}}(t) = \alpha_s e^{-i\omega_s t} \delta_{jm} + \delta \bar{a}_j^{\text{in}}(t), \quad (22)$$

with $\delta \bar{a}_j^{\text{in}}(t)$ satisfying $\langle \delta \bar{a}_j^{\text{in}}(\omega) \delta \bar{a}_l^{\text{in}\dagger}(\omega') \rangle = \delta_{jl} \delta(\omega - \omega')$. In Fourier space, the input field takes the form $\bar{a}_j^{\text{in}}(\omega) = \sqrt{2\pi} \alpha_s \delta(\omega - \omega_s) \delta_{jm} + \delta \bar{a}_j^{\text{in}}(\omega)$, and using this in Eq. (21) we obtain the output field $\bar{a}_j^{\text{out}}(\omega)$ in terms of the Green's functions. It can be decomposed in coherent and incoherent parts, $\bar{a}_j^{\text{out}}(\omega) = \langle \bar{a}_j^{\text{out}}(\omega) \rangle + \delta \bar{a}_j^{\text{out}}(\omega)$, which read

$$\begin{aligned} \langle \bar{a}_j^{\text{out}}(\omega) \rangle = & [\delta_{jm} - i\kappa G_{jm}(\omega_s)] e^{-i\phi(j-m)} \sqrt{2\pi} \alpha_s \delta(\omega - \omega_s) \\ & - i\kappa G_{j,N+m}(-\omega_s) e^{-i\phi(j+m)} \sqrt{2\pi} \alpha_s^* \delta(\omega + \omega_s) \\ & + \sqrt{2\pi} \kappa \alpha e^{-i\phi j} \delta(\omega), \end{aligned} \quad (23)$$

and

$$\begin{aligned} \delta \bar{a}_j^{\text{out}}(\omega) = & \sum_l [\delta_{jl} - i\kappa G_{jl}(\omega)] e^{-i\phi(j-l)} \delta \bar{a}_l^{\text{in}}(\omega) \\ & - i\kappa \sum_l G_{j,N+l}(\omega) e^{-i\phi(j+l)} \delta \bar{a}_l^{\text{in}\dagger}(-\omega). \end{aligned} \quad (24)$$

Using an inverse Fourier transform on Eqs. (23)-(24), we obtain the solution for the output field, which also can be decomposed in coherent and incoherent contributions,

$$\bar{a}_j^{\text{out}}(t) = \langle \bar{a}_j^{\text{out}}(t) \rangle + \delta \bar{a}_j^{\text{out}}(t). \quad (25)$$

The coherent part describes the amplification of the coherent signal, and it is given by

$$\begin{aligned} \langle \bar{a}_j^{\text{out}}(t) \rangle = & [\delta_{jm} - i\kappa G_{jm}(\omega_s)] e^{-i\phi(j-m)} \alpha_s e^{-i\omega_s t} \\ & - i\kappa G_{j,N+m}(-\omega_s) e^{-i\phi(j+m)} \alpha_s^* e^{i\omega_s t} \\ & + \sqrt{\kappa} \alpha e^{-i\phi j}. \end{aligned} \quad (26)$$

The output field does not only contain the amplified signal at frequency $\omega = \omega_s$, but also the idler field at frequency $\omega = -\omega_s$ and the pump at $\omega = 0$. Note that all frequencies are taken with respect to the pump ω_b .

From Eq. (26) we can identify the gain factors that the amplifier provides on the signal and idler fields. In particular, for a input signal entering the device at site 1 and leaving at site $j > 1$, we have

$$\mathcal{G}_j = \kappa^2 |G_{j1}(\omega_s)|^2, \quad (27)$$

$$\mathcal{G}_j^{(I)} = \kappa^2 |G_{j,N+1}(-\omega_s)|^2, \quad (28)$$

where \mathcal{G}_j and $\mathcal{G}_j^{(I)}$ are the signal and idler gains, respectively. In addition, reverse gain is obtained by setting the input at

site $j > 1$ and the output at site 1, so that the field needs to propagate from right to left along the device. We obtain,

$$\mathcal{G}_j^{(R)} = \kappa^2 |G_{1j}(\omega_s)|^2, \quad (29)$$

$$\mathcal{G}_j^{(I,R)} = \kappa^2 |G_{1,N+j}(-\omega_s)|^2, \quad (30)$$

where $\mathcal{G}_j^{(R)}$ and $\mathcal{G}_j^{(I,R)}$ are the signal and idler reverse gains, respectively. When operating the system as a phase-preserving parametric amplifier [4, 53], we measure the output at the same frequency as the signal ω_s and therefore Eqs. (27) and (29) characterize the directional amplification as done in the main text. Nevertheless, the idler field is still amplified at frequency $\omega = -\omega_s$ and this is characterized by Eqs. (28) and (30). Note also that the amplification of the signal field is related to the normal Green function components $G_{jl}(\omega)$ while idler is connected to the anomalous ones $G_{j,N+l}(\omega)$.

The incoherent part of the output field $\delta \bar{a}_j^{\text{out}}(t)$ in Eq. (25) describes the quantum noise added by the amplifier. In particular, the noise flux at output j can be calculated as using Eq. (24) as,

$$N_j = \langle \delta \bar{a}_j^{\text{out}\dagger}(t) \delta \bar{a}_j^{\text{out}}(t) \rangle \quad (31)$$

$$= \frac{1}{2\pi} \iint d\omega d\omega' e^{i(\omega-\omega')t} \langle \delta a_j^{\text{out}\dagger}(\omega) \delta a_j^{\text{out}}(\omega') \rangle \quad (32)$$

$$= \frac{1}{2\pi} \int d\omega n_j(\omega), \quad (33)$$

where $n_j(\omega) = \kappa^2 \sum_l |G_{j,N+l}(\omega)|^2$ is the number of incoherent noise photons that the amplifier generates per unit frequency ω . The added noise $n_j^{\text{add}}(\omega)$ is then defined as the noise normalized by the gain and reads

$$n_j^{\text{add}}(\omega) = \frac{n_j(\omega)}{\mathcal{G}_j(\omega)} = \frac{\sum_l |G_{j,N+l}(\omega)|^2}{|G_{j1}(\omega)|^2}. \quad (34)$$

Finally, we can use Eqs. (21) and Eq. (22) to solve for the dynamics of the fluctuation operators $\delta a_j(t)$ via inverse Fourier transform and, in particular, to determine the photon number occupation of the fluctuations at site j :

$$\begin{aligned} \langle \delta a_j^\dagger(t) \delta a_j(t) \rangle &= \frac{1}{2\pi} \iint d\omega d\omega' e^{i(\omega-\omega')t} \langle \delta a_j^\dagger(\omega) \delta a_j(\omega') \rangle \\ &= \frac{|\alpha_s|^2}{\kappa} \left\{ \mathcal{G}_j + \mathcal{G}_j^{(I)} \right. \\ &\quad \left. + 2\sqrt{\mathcal{G}_j \mathcal{G}_j^{(I)}} \cos(2\omega_s t - \tilde{\Phi}_j) \right\}, \\ &\quad + \frac{1}{2\pi\kappa} \int d\omega n_j(\omega). \end{aligned} \quad (35)$$

As discussed in the main text, the occupation $\langle \delta a_j^\dagger(t) \delta a_j(t) \rangle$ has a coherent contribution proportional to the signal intensity $|\alpha_s|^2$ and also an incoherent contribution given by the total noise flux N_j/κ . Note that the coherent contribution oscillates in time with frequency $2\omega_s$ and constant phase $\tilde{\Phi}_j = 2\varphi_s + 2\phi + \varphi_j - \bar{\varphi}_j$ with φ_s , φ_j , and $\bar{\varphi}_j$ the phases of α_s , $G_{j1}(\omega_s)$ and $G_{j,N+l}(-\omega_s)$, respectively. For $\Delta = 0$, we have $\mathcal{G}_N^{(I)} = \mathcal{G}_N$, and we obtain Eq. (9) of the main text after the a simple maximization of the cosine function.

II.—DIRECTIONAL AMPLIFICATION FROM EDGE STATES OF EXTENDED HAMILTONIAN

In this section, we give details on the fundamental relation between the edge states of the extended Hamiltonian $\mathcal{H}(\omega)$ in Eq. (7) and the topological amplification properties of the system, such as the exponential dependence of the Green's functions. A more extended description of this theoretical framework can be found in our previous work [27].

The starting point of our formalism is the expression of the Green's function matrix $G(\omega) = (\omega - H_{\text{nh}})^{-1}$ by means of the following singular value decomposition (SVD):

$$\omega - H_{\text{nh}} = U(\omega) S(\omega) V^\dagger(\omega). \quad (36)$$

Here, $U(\omega)$, $V(\omega)$, are unitary matrices and $S(\omega)$ is a semi-positive diagonal matrix, $S(\omega)_{nm} = \delta_{nm} E_n(\omega)$. Using this decomposition we can write,

$$\begin{aligned} G(\omega) &= V(\omega) S^{-1}(\omega) U^\dagger(\omega) \\ &= \sum_n E_n^{-1}(\omega) \vec{v}^{(n)}(\omega) \vec{u}^{(n)\dagger}(\omega), \end{aligned} \quad (37)$$

where $E_n(\omega) \geq 0$ are singular values, whereas $\vec{u}^{(n)}(\omega)$ and $\vec{v}^{(n)}(\omega)$ are the associated singular vectors given by the columns of $U(\omega)$ and $V(\omega)$, respectively. As originally demonstrated in Ref. [25], the quantities $E_n(\omega)$, $\vec{v}^{(n)}(\omega)$, and $\vec{u}^{(n)}(\omega)$ can also be interpreted as the positive eigenenergies and the associated eigenvectors of the extended Hamiltonian $\mathcal{H}(\omega)$ defined in Eq. (7). Therefore, the decomposition (37) can also be obtained by solving the eigenvalue problem

$$\mathcal{H}(\omega) \begin{pmatrix} \vec{u}^{(n)} \\ \vec{v}^{(n)} \end{pmatrix} = \pm E_n \begin{pmatrix} \vec{u}^{(n)} \\ \pm \vec{v}^{(n)} \end{pmatrix}. \quad (38)$$

The extended Hamiltonian $\mathcal{H}(\omega)$ has an intrinsic chiral symmetry which may induce to the emergence of zero-energy modes in the spectrum E_n . A crucial observation is that those zero-energy modes lead to the enhancement of the Green's function, since E_n appears inverted in Eq. (37).

Following the reasoning above, the characterization of the spectral amplifying properties of the system can be obtained by exploiting the relation between the Green's function and the eigenstates of the effective Hamiltonian. In particular, we can identify topological amplification regimes in which the extended Hamiltonian $\mathcal{H}(\omega)$ is in a topologically non-trivial phase according to the ten-fold way [35, 36]. In that case, the eigen-spectrum E_n presents at least one pair of zero-energy modes $\pm E_0$ with exponentially small energy, $E_0 \propto e^{-N\zeta}$. Also the associated zero-energy eigenvectors behave as edge states localized either on the right boundary, $v_j^{(0)} \sim v_{N+j}^{(0)} \sim e^{j\zeta}$, or on the left boundary, $u_j^{(0)} \sim u_{N+j}^{(0)} \sim e^{-j\zeta}$, with ζ the inverse localization length. In Fig. 6(a) we present a numerical check of the existence of those localized singular vectors for the same parameters used in Fig. 2 of the main text. Note that

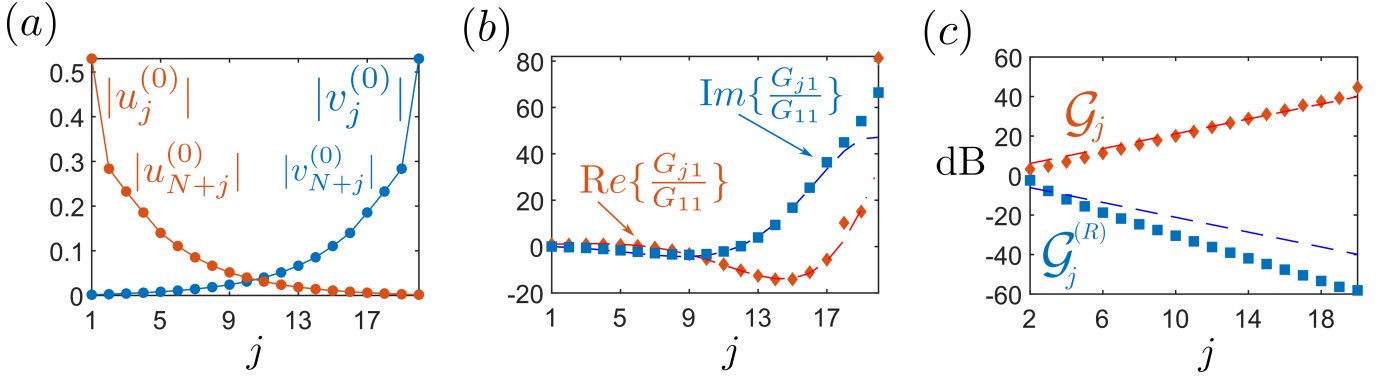


FIG. 6. **Connection between edge states of $\mathcal{H}(\omega)$ and exponential dependence of Green's functions.** (a) Absolute value of edge states $|u_j^{(0)}|$ and $|u_{N+j}^{(0)}|$ (red) and $|v_j^{(0)}|$ and $|v_{N+j}^{(0)}|$ (blue) as function of array site j and for given $\omega = -0.5J$. (b) Real part (red diamonds) and imaginary part (blue squares) of the normalized Green's function G_{j1}/G_{11} as function of site index j . Dashed lines correspond to the exponential fit $G_{j1}/G_{11} = e^{\zeta(j-1)}$ with a localization length $\zeta \approx 0.22 - 0.29i$. (c) Exponential dependence of gain \mathcal{G}_j and reverse gain $\mathcal{G}_j^{(R)}$. Dashed lines correspond to the prediction from the exponential fit in (b). Notice that the fit works well for the gain, but it overestimates the reverse gain (see text). We consider parameter set P_1 with $N = 20$ and $\omega = -0.5J$, as used in Fig. 2 of the main text.

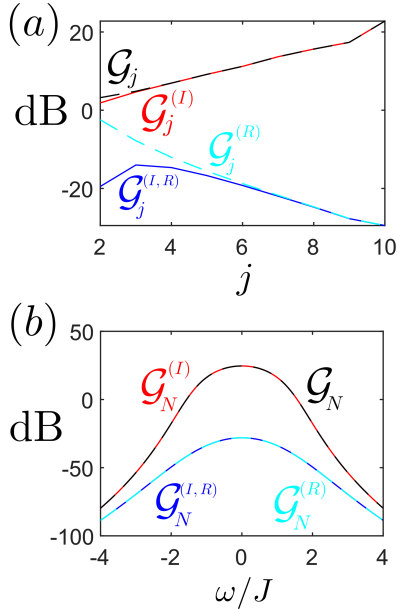


FIG. 7. **Comparison of gain and reverse gain for signal and idler fields.** (a) Spatial dependence of signal gain \mathcal{G}_j (black, dashed), idler gain $\mathcal{G}_j^{(I)}$ (red, dashed), signal reverse gain $\mathcal{G}_j^{(R)}$ (cyan, dashed), and idler reverse gain $\mathcal{G}_j^{(I,R)}$ (blue, solid) as function of array index j , for given frequency $\omega_s = -0.5J$. (b) Frequency dependence of the same quantities, evaluated at the last site $j = N$. Parameters are for operation point P'_1 with $N = 10$.

for these parameters, we have the condition $u_{N+j}^{(0)} = iu_j^{(0)}$ and $v_{j,N+l}^{(0)} = iv_j^{(0)}$ and therefore they overlap in Fig. 6(a).

The exponential suppression with system size of the energy of zero-energy eigenvectors suggests that the first term of the SVD decomposition is the dominant contribution to the

Green's function,

$$G_{jl}(\omega) = E_0^{-1}(\omega)v_j^{(0)}(\omega)u_l^{(0)*}(\omega) + \sum_{n>0} E_n^{-1}(\omega)v_j^{(n)}(\omega)u_l^{(n)*}(\omega). \quad (39)$$

Indeed, for $j > l$, the first term in the right-hand side of Eq. (39) is exponentially larger than the contributions with $n \neq 0$, and therefore the Green's function $G_{jl}(\omega)$ can be well-approximated as stated in the main text, by

$$G_{jl}(\omega) \approx e^{(j-l)\zeta(\omega)}G_{11}(\omega), \quad j > l. \quad (40)$$

This occurs analogously for the anomalous components $G_{j,N+l}(\omega)$ when $j > l$. In Fig. 6(b) we numerically confirm this approximation by performing an exponential fit to the real and imaginary parts of the normalized Green's function components G_{j1}/G_{11} , numerically calculated with the expression $G_{jl} = (\omega - H_{\text{nh}})^{-1}$. We see that the fit $G_{j1}/G_{11} = e^{\zeta(j-1)}$ with $\zeta \approx 0.22 - 0.29i$ agrees very well with the numerical data, up to finite size effects near the boundary $j = N$ [cf. dashed lines in Fig. 6(b)].

The exponential dependence of $G_{j1}(\omega)$ also implies that the topological amplifier's gain grows exponentially $\mathcal{G}_j = \kappa^2 |G_{j1}(\omega)|^2 \sim e^{2\zeta(j-1)} |G_{11}(\omega)|^2$. In Fig. 6(c) we show that the gain grows exponentially very close to the theoretical prediction [cf. red diamonds and dashed line in Fig. 6(c)].

Note, however, that in our numerical calculations [cf. blue squares and dashed line in Fig. 6(c)], the reverse gain $\mathcal{G}_j^{(R)}$ turns out to be even lower than the decreasing exponential scaling $\propto e^{-2\zeta(j-1)}$ that one would naively expect. The reason for this lies in the decomposition (39). For $j < l$, the first term $\sim E_0^{-1}$ shows indeed the exponential dependence $\sim e^{-\zeta|j-l|}$, but this exponentially suppressed term does not dominate the behaviour of G_{jl} , as it is on the same order as the sum of all the others. We have found numerically that, remarkably, contributions from singular vectors with $n \neq 0$

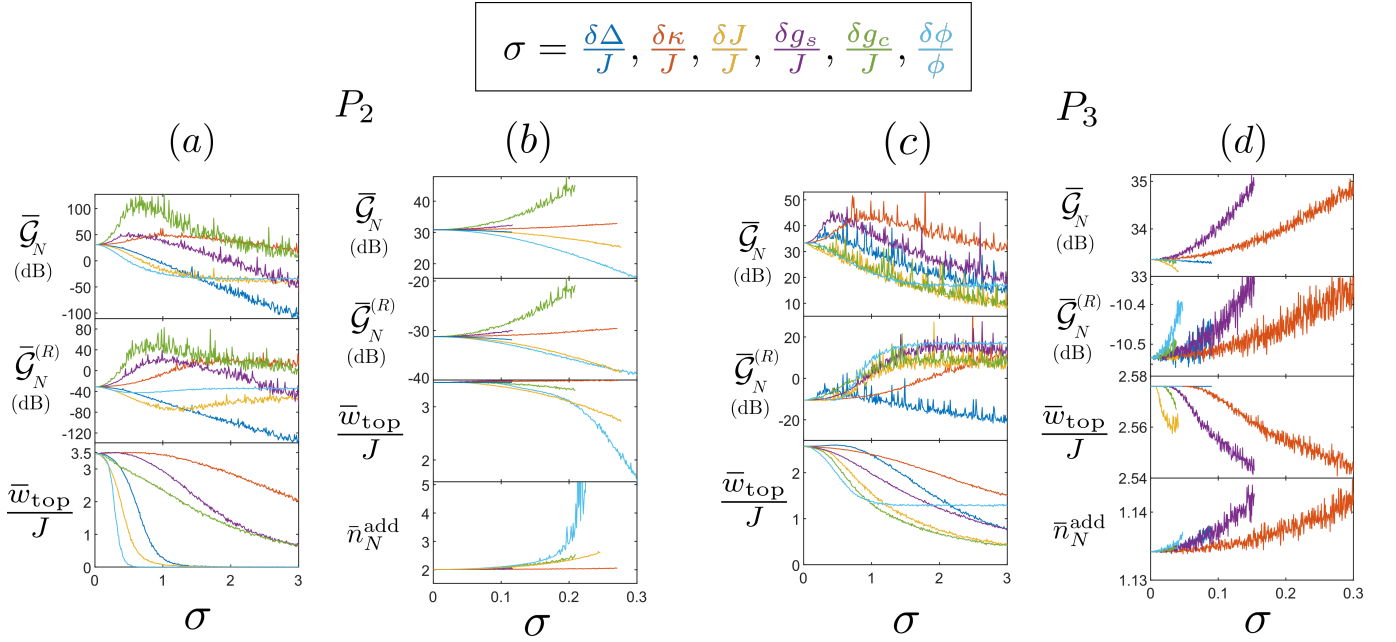


FIG. 8. **Robustness to disorder for operation points P_2 and P_3 .** (a)-(b) Average gain \bar{G}_N , reverse gain $\bar{G}_N^{(R)}$, topological bandwidth \bar{w}_{top}/J , and added noise \bar{n}_N^{add} as function of the dimensionless disorder strength σ , defined for each effective system parameter as $\sigma = \delta\Delta/J$ (blue), $\sigma = \delta\kappa/J$ (red), $\sigma = \delta J/J$ (yellow), $\sigma = \delta g_s/J$ (purple), $\sigma = \delta g_c/J$ (green), and $\sigma = \delta\phi/\phi$ (cyan). All quantities are averaged over 1000 realizations for each type of disorder around the mean values defined by parameters P_2 . Panel (b) is a zoom of (a) for $\sigma \leq 0.3$ and the termination of certain curves indicate the disorder at which the steady-state becomes unstable. (c)-(d) show the same quantities as (a)-(b), but for mean parameters P_3 . The frequency of the input signal is set to $\omega_s = -0.5J$ in all cases.

interfere destructively with each other, resulting in a reverse gain that is even more suppressed than one can expect from the exponential dependence of the edge states alone [cf. Fig. 6(c)]. Therefore, increasing the array size N is doubly beneficial since it enhances exponentially both directional amplification and suppression of backward emission.

Finally, we comment that the behaviour for the idler field at frequency $\omega = -\omega_s$ is qualitatively equal as what is shown in the main text for the signal field at $\omega = \omega_s$. In particular, when $\Delta = 0$, we see that $G_{j,N+l} = iG_{jl}$ and therefore G_j and $G_j^{(R)}$ are equivalent to $G_j^{(I)}$ and $G_j^{(R,I)}$, up to finite size effects at the boundaries. We present a numerical check of this result in Fig. 7(a)-(b), where we show the spatial and frequency dependence of all these quantities for the same parameters as Fig. 2 of the main text.

III.— TOPOLOGICAL PROTECTION TO DISORDER AT OPERATION POINTS P_2 AND P_3

The main features of the topological protection against disorder are discussed in the main text on the example of the operation point P'_1 of the amplifier. The results are qualitatively similar for operation points P_2 and P_3 , but there are some quantitative differences, specially regarding the stability, which we shortly address here.

The complete data is shown in Figs. 8(a)-(d). Here, for an input signal of frequency $\omega_s = -0.5J$, we display the aver-

age gain \bar{G}_N , reverse gain $\bar{G}_N^{(R)}$, topological bandwidth \bar{w}_{top} , and added noise \bar{n}_N^{add} as function of the dimensionless disorder strength for all effective system parameters defined as $\sigma = \delta\Delta/J$ (blue), $\sigma = \delta\kappa/J$ (red), $\sigma = \delta J/J$ (yellow), $\sigma = \delta g_s/J$ (purple), $\sigma = \delta g_c/J$ (green), and $\sigma = \delta\phi/\phi$ (cyan). Panels (a)-(b) correspond to the operation point P_2 , while panels (c)-(d) correspond to P_3 . In addition, panels (b) and (d) are a zoom of panels (a) and (c), respectively, where we show in more detail the behaviour of the average quantities for $\sigma \leq 0.3$. In these zoom panels (b) and (d) the ending of a curve before $\sigma = 0.3$ indicates the disorder strength at which the steady-state becomes unstable (i.e. when the imaginary part of at least one eigenvalue of H_{nh} becomes positive).

First we discuss the operation point P_2 as it is the most similar to P'_1 : We see that disorder in δg_s (purple), δg_c (green), and δJ (red) increase the gain \bar{G}_N and reverse gain $\bar{G}_N^{(R)}$ for $\sigma \leq 1$. This enhances the amplification but reduces the directionality. For $\sigma \gg 1$, all types of disorder destroy the topological properties of the amplification as they reduce gain, reverse gain, and topological bandwidth, while increasing added noise, analogously as what happens for P'_1 . The main difference in the behavior between operation points P_2 and P'_1 is that amplifier at P_2 becomes unstable at a slightly lower disorder due to the larger proximity to the instability region in Fig. 4 of the main text. However, we still see for both cases the system is robust up to a disorder strength $\sigma \lesssim 0.1$ in all system parameters, with minimum change in the overall amplifying performance, including a minimum increase in added

noise.

In the case of P_3 , disorder in δg_s , $\delta \kappa$, and $\delta \Delta$ increase the gain for moderate disorder $\sigma \lesssim 1$, and then for $\sigma \gg 1$ all types of disorder reduce it. Interestingly, amplification is still maintained with up to 10 dB of gain for a large disorder of $\sigma \sim 3$. Nevertheless, such a large disorder destroys the directionality of the device by making the reverse gain positive (except for disorder in $\delta \Delta$). As for P'_1 and P_2 , disorder in all parameters reduce topological bandwidth and increase added noise. It is curious to note that a large disorder in $\delta \phi$ does not

reduce \bar{w}_{top} to zero, but it saturates at a finite value. However, that behaviour is not possible to be observed in practice since the system becomes unstable at a much lower disorder of $\delta \phi / \phi \sim 0.5$ for the case of phase. In general, the amplifier at the operation point P_3 is much more unstable than at points P'_1 and P_2 due to its proximity to the unstable region and also for having a larger inverse localization length $\text{Re}[\zeta] \sim 1$. This makes the amplifier behavior more susceptible to small changes in parameters. However, we see that the topological amplifier at this point is still robust to a disorder of order 3% in all system parameters.